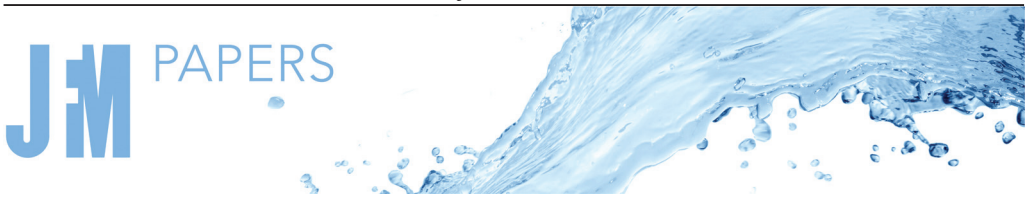
J. Fluid Mech. (2021), *vol*. 920, A28, doi:10.1017/jfm.2021.448



Direct numerical simulation of roughness-induced transition controlled by two-dimensional wall blowing

Yuhan Lu[1], **Fanzhi Zeng**[1], **Hongkang Liu**[2], **Zaijie Liu**[1] **and Chao Yan**[1,†]

[1]National Key Laboratory of Computational Fluid Dynamics, Beihang University, Beijing 100191, PR China

[2]Key Laboratory of Traffic Safety on Track, Ministry of Education, School of Traffic and Transportation Engineering, Central South University, Changsha 410075, PR China

(Received 15 December 2020; revised 18 April 2021; accepted 10 May 2021)

Discrete roughness-induced transition in Mach 2.25 flow controlled by two-dimensional wall blowing is studied using direct numerical simulation. Spectral analysis and flow freezing operations reveal that the main source of unsteadiness in the case without blowing is the separated shear layer/counter-rotating vortex system: the shear layer is bent by the vortex pair, and this interaction induces disturbance growth at the shear layer. With the existence of weak wall blowing, the transition is delayed. Flow visualization demonstrates that upstream-positioned blowing achieves this by lifting the inflow boundary layer and decreasing the roughness Reynolds number. In contrast, downstream-positioned blowing takes effect by weakening the counter-rotating vortex pair and inhibiting the interaction. Vorticity transportation analysis suggests that this result is accomplished by increasing dissipation for streamwise vorticity and converting some of it into spanwise vorticity. In cases with strong wall blowing, the control effect is reversed, as wall blowing with enough strength can induce unsteadiness and promote transition. In upstream-positioned strong blowing cases, a new unstable mode is observed in spectral results throughout the near-roughness region, and further analysis indicates that this mode originating from the separation zone upstream of the blowing is the key factor for transition. With regard to downstream-positioned strong blowing cases, a very low-frequency mode is generated from the separation bubble between the roughness element and the blowing, but it only provides an initial disturbance for the transition process. The transition that occurs downstream is due to the distortion of the boundary layer in the wake.

Key words: transition to turbulence, instability control, compressible boundary layers

† Email address for correspondence: yanchao@buaa.edu.cn

© The Author(s), 2021. Published by Cambridge University Press

https://doi.org/10.1017/jfm.2021.448 Published online by Cambridge University Press

1. Introduction

With the development of high-speed aircraft, there is growing concern over the laminar–turbulent transition. As roughness-induced transition is one of the main forms of transition for high-speed vehicles, its control is of great importance for the reduction of surface heat flux and friction drag (Lin 2008; Estruch-Samper *et al.* 2017). To obtain an effective approach for the control of roughness-induced transition, its mechanism should first be understood. However, although massive efforts have been made, it is still not well known, and a substantial amount of work needs to be done (Schneider 2015). Early researchers (Smith & Clutter 1959) indicated that whether or not the transition occurs downstream depends on the properties of the boundary layer at the maximum height of roughness element k_r, and, therefore, the roughness Reynolds number Re_{kk} was defined to predict transition:

$$Re_{kk} = \frac{\rho_k u_k k_r}{\mu_k}. \tag{1.1}$$

Here ρ, u and μ are density, streamwise velocity and dynamic viscosity, respectively, and subscript k represents quantities measured at k_r. The transition onset position will rapidly approach the roughness when Re_{kk} exceeds a critical value (Puckert & Rist 2018). While the roughness Reynolds number is an effective criterion for transition prediction in cases where the roughness element is overwhelmed by the boundary layer (Bernardini *et al.* 2014), it remains a phenomenological theory.

Previous attempts to describe the mechanism of roughness-induced transition suggested that the source of unsteadiness varies with the change in flow configuration. There are several main structures in the flow past the roughness element that may introduce disturbance into flow fields. In the upstream separation zone, there is a horseshoe vortex formed wrapping around the front half of the roughness, and then it trails downstream as streamwise vortices (Gregory & Walker 1956). Baker (1979) conducted a thorough investigation of the horseshoe vortex system in a laminar separation zone upstream of the roughness element. Especially in cases with a high roughness element relative to the boundary layer displacement thickness, complicated unsteady behaviour was found resulting from the instability of the vortex system itself.

In the high-speed boundary layer, a shockwave system exists in front of the roughness. It was observed by Subbareddy, Bartkowicz & Candler (2014) that the vortex system in the separation zone perturbs the shockwave by affecting the compression wave system near the wall. Moreover, disturbance in the downstream wake structure also influences the shockwave through the boundary layer. They indicated that the upstream vortex and shockwave systems are the primary causes of transition occurring downstream of a cylindrical roughness at inflow Mach number $Ma_\infty = 6$ (Ma is the Mach number, and subscript ∞ refers to quantities of inflow).

The shear layer shedding from roughness can also be a main contribution to the disturbance growth, as it can create an inflection point in the velocity profile and introduce Kelvin–Helmholtz (KH) instability into the flow field (Ergin & White 2006; Semper & Bowersox 2017). Hamed *et al.* (2016) observed in experiments that fluctuation near roughness is related to the shear layer separated from both two-dimensional and three-dimensional periodic roughness, and Chou, Kegerise & King (2020) found that the shear layer can induce sinuous or varicose mode instabilities depending on the roughness height.

Except for the shear layer, the wake structure also contains a counter-rotating vortex pair shedding from the top of the roughness element (Gregory & Walker 1956).

https://doi.org/10.1017/jfm.2021.448 Published online by Cambridge University Press

The lift-up effect (Landahl 1980; Brandt 2014) allows streamwise vortices in the wake to induce disturbance transient growth (Reshotko 2001) by distorting the boundary layer profile in the spanwise direction and creating streaks, which is the optimal disturbance in transient growth mechanisms according to the results of theory (Luchini 2000). Experiments performed by White (2002) and White, Rice & Ergin (2005) indicated that disturbance undergoes an algebraic transient growth at the position of streamwise vortices behind an isolated roughness element and finally results in transition downstream.

Moreover, the counter-rotating vortex pair can interact with a separated shear layer and bend it to surround the wake (De Tullio *et al.* 2013). As observed by Muppidi & Mahesh (2012) in flow at $Ma_\infty = 2.9$ past distributed roughness, the interaction between these two structures can lead to the shear layer breaking down into turbulence. In cases with isolated cylindrical roughness, Subbareddy *et al.* (2014) recognized the interaction as the second dominant mechanism of transition using dynamic mode decomposition (DMD) (Rowley *et al.* 2009; Schmid 2010). Recently, Shrestha & Candler (2019) performed a similar analysis on flow past a diamond-shaped roughness, and suggested that the separated shear layer/counter-rotating vortex interaction is the primary cause for transition in their study.

As roughness-induced transition is a competitive mechanism between the development of unsteady fluctuation and relaxation of flow field distortion (Ergin & White 2006), the studies above seem to imply that the roughness-induced transition can be controlled by changing the magnitude of these main structures in the flow field and influencing the growth rate of the disturbance. For example, White *et al.* (2005) observed that the change in the roughness configuration alters the vorticity field in the wake structure and affects the disturbance transient growth rate, and Subbareddy *et al.* (2014) found that the inflow Reynolds number has an important impact on the structure of the horseshoe vortex system in the upstream separation zone and the transition onset position downstream of cylindrical roughness.

Thus, several effective control methods have been proposed to modify the flow configuration of the roughness-disturbed boundary layer. One of them delays transition by placing another roughness element with a specially designed shape at a specific position downstream of the original element, so that the distortion of the boundary layer profile generated by these two elements can counteract each other. This method was first adopted for two-dimensional roughness by Kobayashi *et al.* (1994) and then applied to the control of three-dimensional roughness (Sharma *et al.* 2014; Suryanarayanan *et al.* 2017). Despite its significant effect, this method only works on roughness with a particular shape. Another method takes effect with some relatively lower roughness around the original one. The phenomenon of this method was first observed by Kendall (1981) and then employed in the control of the transition induced by distributed (Downs, White & Denissen 2008) and discrete roughness (Kuester & White 2015). Lu *et al.* (2020*a*,*b*) analysed the effect of upstream and downstream-positioned control roughness separately and argued that their roles in transition control are different. However, as a passive strategy, it is unable to adjust the control effect. Moreover, the small-amplitude roughness used in this method would not only introduce some additional disturbance into the flow field but also increase surface friction and heat flux, especially in the high-speed boundary layer.

Wall blowing is a widely used and adjustable tool in the control of transition induced by first-mode instabilities (Sharma *et al.* 2019), and it is reported to have the ability to reduce surface friction drag (Mori, Quadrio & Fukagata 2017). Therefore, our aim is to propose a new method for the control of transition induced by roughness using wall blowing. Direct numerical simulation (DNS) is performed in this paper to obtain an accurate flow field of the transition process so that the mechanism of roughness-induced transition and its control with wall blowing can be analysed. Wall blowing located both upstream and

https://doi.org/10.1017/jfm.2021.448 Published online by Cambridge University Press

Ma_∞	Re_{ref} (m^{-1})	T_∞ (K)	T_w (K)	R	γ	Pr
2.25	2.5×10^7	169.44	322	287.2	1.4	0.72

Table 1. Free-stream flow conditions.

downstream of the roughness element is studied separately, as their roles in the control of roughness-induced transition seem to be different. Furthermore, blowing of weak or strong intensity is simulated separately because they have a reverse influence on the transition onset position with the increase in intensity.

This paper is organized as follows. In § 2 we illustrate the set-up of our computations and the validation of our results. Then in § 3 we demonstrate the results of all the cases and our analyses. The mechanism of transition induced by a discrete roughness element is analysed in § 3.1, the role of upstream- or downstream-positioned weak wall blowing in the inhibition of transition is assessed in § 3.2, and the effect of upstream- or downstream-positioned strong wall blowing promoting transition is investigated in § 3.3. Finally, § 4 presents the conclusion of our study.

2. Computation set-up and validation

In this paper, a supersonic free-stream flow condition is considered for all cases. The inflow parameters are described in table 1 (where $Re_{ref} = \rho_\infty u_\infty/\mu_\infty$, T represents temperature, subscript w denotes flow parameters at the wall, and R, γ and Pr are the gas constant, heat capacity ratio and laminar Prandtl number, respectively). This condition has been adopted in many studies before (Pirozzoli, Grasso & Gatski 2004; Li *et al.* 2009).

As mentioned in § 1, the roughness Reynolds number Re_{kk} is a key parameter for roughness-induced transition. In this study, a discrete roughness element is placed at $x_r = 101.6$ mm (measured from the leading edge of the flat plate). To estimate the maximum height of the roughness element to satisfy the given value of Re_{kk}, we need to obtain the flow profile at x_r in the undisturbed laminar boundary layer. For this purpose, compressible Blasius equations (Stewartson 1964) are solved with the shooting method and eighth-order Runge–Kutta method (Butcher 2003). The compressible Blasius equations with similarity transformation can be written as

$$\left.\begin{gathered}\frac{\mathrm{d}}{\mathrm{d}\eta_c}\left(\frac{\rho\mu}{\rho_\infty\mu_\infty}\frac{\mathrm{d}^2 f}{\mathrm{d}\eta_c^2}\right)+f\frac{\mathrm{d}^2 f}{\mathrm{d}\eta_c^2}=0,\\ \frac{\mathrm{d}}{\mathrm{d}\eta_c}\left(\frac{\rho\mu}{\rho_\infty\mu_\infty}\frac{\mathrm{d}g}{\mathrm{d}\eta_c}\right)+Prf\frac{\mathrm{d}g}{\mathrm{d}\eta_c}+Pr(\gamma-1)Ma_\infty^2\frac{\rho\mu}{\rho_\infty\mu_\infty}\frac{\mathrm{d}^2 f}{\mathrm{d}\eta_c^2}=0,\\ f(0)=\left.\frac{\mathrm{d}f}{\mathrm{d}\eta_c}\right|_{\eta_c=0}=0,\quad g(0)=\frac{T_w}{T_\infty},\quad \lim_{\eta_c\to+\infty}\frac{\mathrm{d}f}{\mathrm{d}\eta_c}=\lim_{\eta_c\to+\infty}g(\eta_c)=1,\end{gathered}\right\} \tag{2.1}$$

where

$$\frac{\mathrm{d}f}{\mathrm{d}\eta_c}=\frac{u}{u_\infty},\quad g=\frac{T}{T_\infty},\quad \eta_c=\sqrt{\frac{\rho_\infty u_\infty}{2\mu_\infty x}}\int_0^y\frac{\rho}{\rho_\infty}\,\mathrm{d}y. \tag{2.2a–c}$$

For all the cases in this paper, the value of the roughness Reynolds number is set to $Re_{kk} = 420$, and therefore the maximum height of the roughness element is

https://doi.org/10.1017/jfm.2021.448 Published online by Cambridge University Press

$L_{x,99}/k_r$	$L_{z,99}/k_r$	h	σ_x	R_x	σ_z	R_z
12.0	12.0	3.18×10^{-2}	9.07×10^{3}	1.02×10^{-3}	9.07×10^{3}	1.02×10^{-3}

Table 2. Shape parameters for smooth-edged roughness element.

Case	$(x_{blow} - x_r)/\delta_r$	L_{blow}/k_r	I_{blow}	$n_x \times n_y \times n_z$
V_0	—	—	0	$1404 \times 104 \times 260$
$X_{-4}V_2$	-4	2	0.02	$1476 \times 104 \times 260$
$X_{-4}V_4$	-4	2	0.04	$1476 \times 104 \times 260$
X_4V_2	$+4$	2	0.02	$1452 \times 104 \times 260$
X_4V_4	$+4$	2	0.04	$1452 \times 104 \times 260$
$X_{-4}V_{18}$	-4	2	0.18	$1476 \times 104 \times 260$
$X_{-4}V_{20}$	-4	2	0.20	$1476 \times 104 \times 260$
X_4V_{23}	$+4$	2	0.23	$1452 \times 104 \times 260$
X_4V_{25}	$+4$	2	0.25	$1452 \times 104 \times 260$

Table 3. Details of all cases in this paper.

$k_r = 0.127$ mm. In addition, from the profile at x_r, we can also obtain that the undisturbed laminar boundary layer thickness at this position is $\delta_r = 0.444$ mm.

The shape function of the smooth-edged roughness element employed in this study is as follows (Balakumar & Kegerise 2016):

$$\left.\begin{aligned} y_{2d}(x) &= h\left\{\tanh\left[\sigma_x\left(\frac{R_x}{2} - x\right)\right] + \tanh\left[\sigma_x\left(\frac{R_x}{2} + x\right)\right]\right\}, \\ y_w(x,z) &= y_2d(x)\left\{\tanh\left[\sigma_z\left(\frac{R_z}{2} - z\right)\right] + \tanh\left[\sigma_z\left(\frac{R_z}{2} + z\right)\right]\right\}, \end{aligned}\right\} \tag{2.3}$$

and the parameters in (2.3) are listed in table 2 (where $L_{x,99}$ and $L_{z,99}$ are the size of the roughness element in the streamwise and spanwise directions defined at the height of $0.01k_r$, respectively).

A slot of two-dimensional wall blowing is placed at $x_{blow} - x_r = \mp 4\delta_r$ for upstream or downstream blowing position cases, and the width of the slot is $L_{blow} = 2k_r$. The formula for the profile of wall blowing is

$$\rho_w v_w(x) = \frac{I_{blow}}{2}\rho_\infty u_\infty\left[\cos\frac{2\pi(x - x_{blow})}{L_{blow}} + 1\right], \tag{2.4}$$

where v is the wall-normal velocity and $I_{blow} = (\rho_w v_w)_{max}/\rho_\infty u_\infty$ represents the intensity of blowing. For the cases simulated in this paper, different values of I_{blow} are employed. Parameters for wall blowing and the grid dimensions of all the cases are reported in table 3 (where $n_x \times n_y \times n_z$ are the number of grid points in the three directions).

The configuration of the computational domain is illustrated in figure 1. The size of the well-resolved region in the computational domain is $L_x \times L_y \times L_z = 150\delta_r \times 28.6\delta_r \times 10\delta_r$. The inlet boundary is placed at $x_{in} - x_r = -50\delta_r$. At the end of the domain, there is a sponge region where the grid is gradually coarsened in the streamwise direction in order to dissipate spurious wave reflections generated at the outlet boundary. The length of the sponge region is $x_{sponge} = 50\delta_r$.

https://doi.org/10.1017/jfm.2021.448 Published online by Cambridge University Press

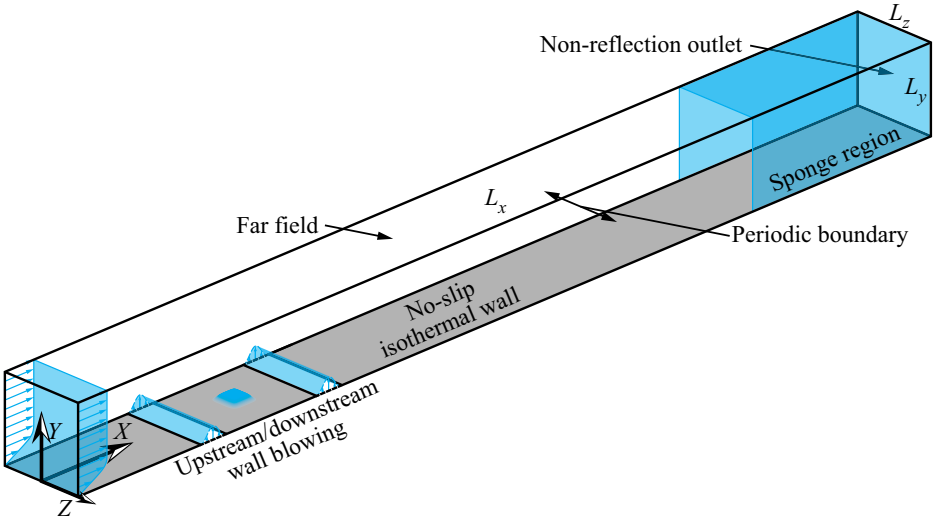


Figure 1. Computational domain configuration.

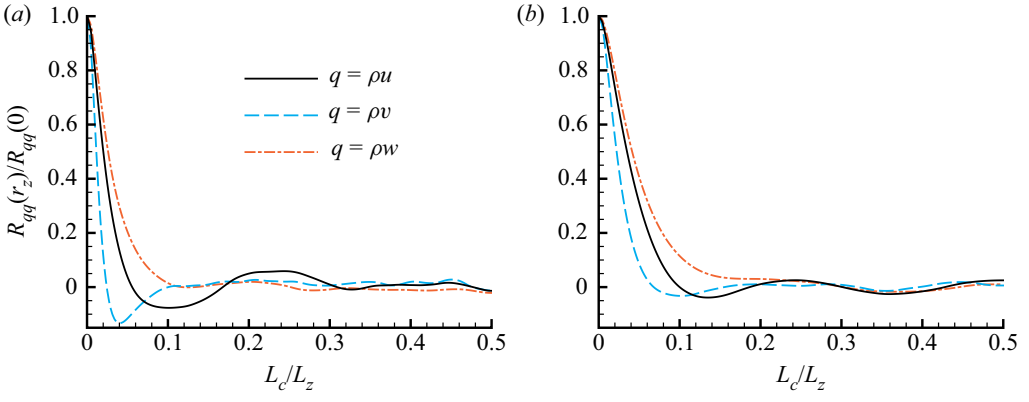


Figure 2. Spanwise correlation coefficients at $x - x_r = 95\delta_r$ and (*a*) $y = k_r$ or (*b*) $y = \delta_r$.

Values of L_y and L_z are referenced to Pirozzoli *et al.* (2004). To verify whether the width of domain L_z is large enough, correlation coefficients in the spanwise direction are analysed. The correlation for quantity q is defined as (Pirozzoli *et al.* 2004)

$$R_{qq}(L_c) = \sum_{k=1}^{n_z-1} \overline{q'_k q'_{k+k_c}}, \tag{2.5}$$

where $\bar{q}$ is the Reynolds average of quantity q, $q' = q - \bar{q}$ represents the fluctuations and $L_c = k_c L_z/n_z$ is the distance between two points. The spanwise correlation coefficients at two different positions are shown in figure 2. It is clear that coefficients for the three components of the momentum vector at these two positions reduce rapidly within $L_c < 0.1L_z$ and approach zero beyond that distance.

At the inlet boundary, a compressible laminar boundary layer profile also obtained by solving (2.1) is imposed. A comparison is presented in figure 3 between two-dimensional DNS results and solutions of compressible Blasius equations with the similarity

https://doi.org/10.1017/jfm.2021.448 Published online by Cambridge University Press

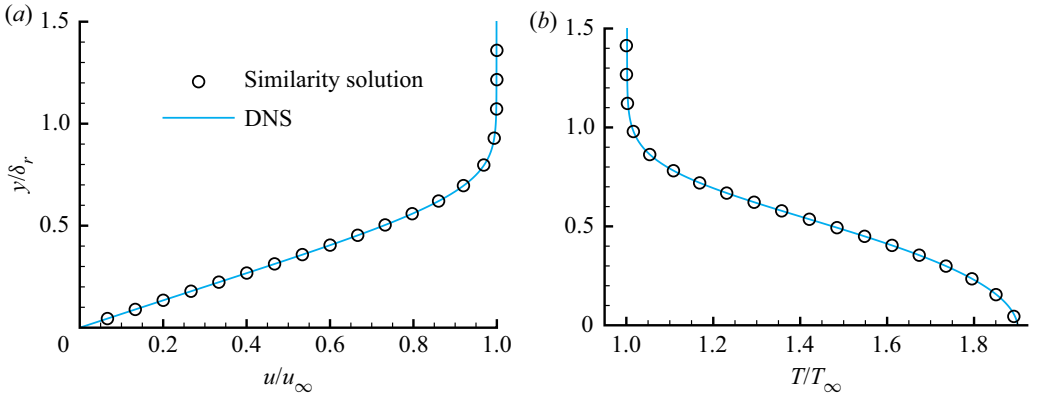


Figure 3. Validation of similarity solution used as the inlet boundary profile: (*a*) streamwise velocity u and (*b*) temperature T.

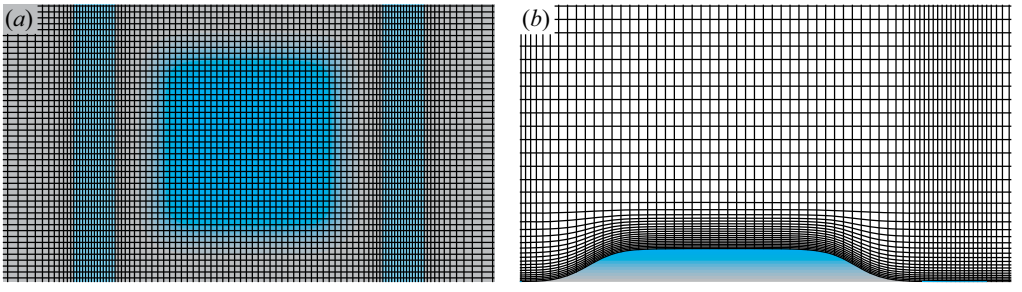


Figure 4. Grid point distributions on (*a*) wall boundary and (*b*) axial plane (displaying every second grid point in each direction).

transformation to validate the inlet boundary profile. As is apparent, the similarity solution is in exceptional agreement with the DNS result. For the two lateral boundaries of the domain, the periodic condition is employed, and the non-slip isothermal wall condition is adopted for the wall boundary along with the boundary layer equation $\partial p/\partial \boldsymbol{n} = 0$ (here p is the static pressure and $\boldsymbol{n}$ denotes the wall-normal vector). In addition, a non-reflecting boundary condition (Poinsot & Lele 1992; Pirozzoli, Grasso & D'Andrea 2001) is used for the upper boundary, and a pressure outlet condition (Pirozzoli *et al.* 2004) is employed for the outlet boundary.

The grid resolution for all the cases is $\Delta x^+ \times \Delta y_w^+ \times \Delta z^+ = 14.45 \times 0.98 \times 6.45$ (dimensionless grid size is defined as $\Delta x_i^+ = \sqrt{\tau_w \rho_w}\Delta x_i/\mu_w$, where τ_w is the wall shear stress and Δx_i represents the grid size in direction i), which is basically the same as in Pirozzoli *et al.* (2004) (see table 4). In regions over the roughness element or the blowing slot, the grid is refined to provide a better description. The distributions of grid points in the near region of the roughness and slot are demonstrated in figure 4.

A grid sensitivity study is also conducted to verify the grid dimension, and the reference cases are reported in table 4. For the cases with subscript *fine*, the mesh is refined in all three directions based on the original cases. A comparison of Reynolds- and spanwise-averaged skin friction distributions between case V_0 and case X_4V_2 is plotted in figure 5(*a*). The skin friction formula given by White & Christoph (1972) is employed

https://doi.org/10.1017/jfm.2021.448 Published online by Cambridge University Press

Case	$n_x \times n_y \times n_z$	$(L_x \times L_y \times L_z)/\delta_r$	$\Delta x^+ \times \Delta y_w^+ \times \Delta z^+$
Pirozzoli *et al.* (2004)	2269 × 56 × 255	286 × 28.6 × 10	14.50 × 1.05 × 6.56
Li *et al.* (2009)	2193 × 72 × 256	320 × 11.3 × 10	14.10 × 1.10 × 6.60
V_0	1404 × 104 × 260	150 × 28.6 × 10	14.45 × 0.98 × 6.45
$V_{0,fine}$	1984 × 147 × 368	150 × 28.6 × 10	10.05 × 0.96 × 4.55
$X_{-4}V_{2,fine}$	2076 × 147 × 368	150 × 28.6 × 10	10.05 × 0.96 × 4.55
$X_4V_{2,fine}$	2032 × 147 × 368	150 × 28.6 × 10	10.05 × 0.96 × 4.55

Table 4. Grid resolution and sensitivity study.

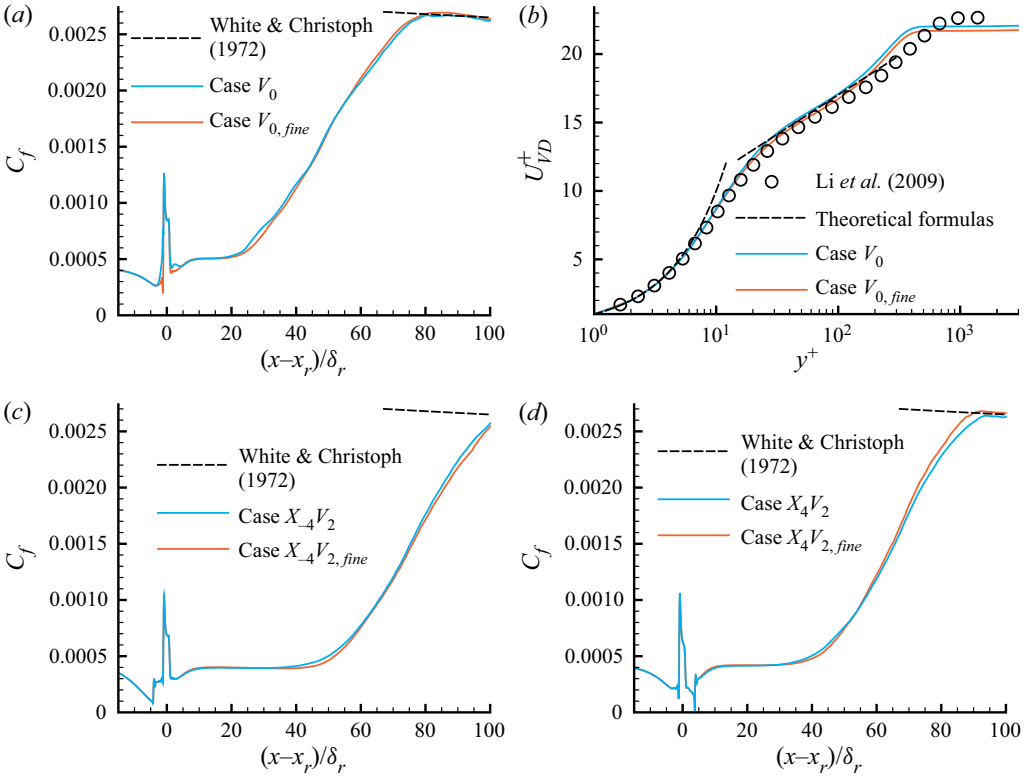


Figure 5. Grid sensitivity study and result validation: skin friction distributions of (*a*) case V_0, (*c*) case $X_{-4}V_2$ and (*d*) case X_4V_2, and (*b*) van Driest velocity profiles at $x - x_r = 95\delta_r$ of case V_0.

as a reference:

$$C_f = \frac{0.455}{S^2}\ln^{-2}\left(\frac{0.06xRe_{ref}}{S\bar{\mu}_w/\mu_\infty}\sqrt{\frac{T_\infty}{T_w}}\right), \quad S = \frac{\sqrt{T_w/T_\infty - 1}}{\arcsin A}, \quad A = \sqrt{\frac{(\gamma-1)Ma_\infty^2}{2T_w/T_\infty}}. \tag{2.6a–c}$$

The results show a good agreement between the two cases. Moreover, the skin friction coefficients of both cases in the fully developed turbulence region correspond well to the theoretical estimate formula.

https://doi.org/10.1017/jfm.2021.448 Published online by Cambridge University Press

In figure 5(*b*), the Reynolds- and spanwise-averaged van Driest velocity U_{VD}^{+} (van Driest 1951) profiles of both cases at $x - x_r = 95\delta_r$ are compared with results from Li *et al.* (2009), where

$$y^{+}=\frac{\rho_w u_\tau y}{\mu_w}, \quad U_{VD}^{+}=\frac{U_{VD}}{u_\tau}, \quad u_\tau=\sqrt{\frac{\tau_w}{\rho_w}}, \quad U_{VD}=\int_0^u \sqrt{\frac{\rho}{\rho_w}}\,\mathrm{d}u. \tag{2.7a–d}$$

In addition, the theoretical formulae – the viscous sublayer linear solution $U_{VD}^{+}=y^{+}$ and the logarithmic layer solution $U_{VD}^{+}=2.5\ln y^{+}+5.5$ (Coles 1956) – are also given for reference purposes. As can be seen, the results for case V_0 agree well with all the reference values in both the inner layer and the log layer. The discrepancy in the wake layer is mainly because the position where we obtain the profile differs from that in Li *et al.* (2009), and as a result the boundary layer thickness is different. The results in figure 5 indicate that the grid resolution is fine enough to deliver a good accuracy for DNS of roughness-induced transition.

Besides, the skin frictions of case $X_{-4}V_2$ and case X_4V_2 are also compared with their corresponding reference cases, respectively (see figures 5*a* and 5*b*). The results show that the mesh employed in our study can also describe the influence of wall blowing well enough.

In this paper, the unsteady compressible Navier–Stokes equations are employed as the governing equations:

$$\frac{\partial \boldsymbol{Q}}{\partial t}+\frac{\partial \boldsymbol{F}_{c,j}}{\partial x_j}=\frac{\partial \boldsymbol{F}_{v,j}}{\partial x_j} \quad (j=1,2,3), \tag{2.8}$$

where $\boldsymbol{Q}$ is the vector of conservative variables, and $\boldsymbol{F}_{c,j}$ and $\boldsymbol{F}_{v,j}$ represent convective and viscous flux vectors in three directions, respectively. They can be calculated as

$$\left.\begin{gathered}\boldsymbol{Q}=\begin{pmatrix}\rho\\ \rho u_i\\ \rho e\end{pmatrix}, \quad \boldsymbol{F}_{c,j}=\begin{pmatrix}\rho u_j\\ \rho u_i u_j+p\delta_{ij}\\ (\rho e+p)u_j\end{pmatrix}, \quad \boldsymbol{F}_{v,j}=\begin{pmatrix}0\\ \sigma_{ij}\\ \sigma_{ij}u_i+q_j\end{pmatrix}, \quad (i,j=1,2,3),\\ e=\frac{p}{(\gamma-1)\rho}+\frac{u_i^2}{2}, \quad \sigma_{ij}=\begin{cases}\mu\left(\dfrac{\partial u_j}{\partial x_i}+\dfrac{\partial u_i}{\partial x_j}\right), & i\neq j,\\ 2\mu\dfrac{\partial u_i}{\partial x_i}-\dfrac{2}{3}\mu\boldsymbol{\nabla}\cdot\boldsymbol{u}, & i=j,\end{cases} \quad q_i=k\frac{\partial T}{\partial x_j},\end{gathered}\right\} \tag{2.9}$$

where δ_{ij} is the Kronecker delta, $\boldsymbol{u}$ represents the velocity vector and k is the thermal conductivity.

To solve the body-fitted mesh that describes the shape of the smooth-edged roughness element, governing equations in curvilinear coordinates (Deng *et al.* 2011) are employed. In this paper, the governing equation is solved with the finite-difference code OpenCFD developed by Li *et al.* (2010). The parallel code has been proven to be reliable in multiple studies (Li *et al.* 2009; Lu *et al.* 2020*a*,*b*). For the spatial discretization of the convective terms, the WENO-SYMBO method (Martin *et al.* 2006) with Steger–Warming splitting (Steger & Warming 1981) is used. The viscous terms are computed with an eighth-order central-differencing scheme. A third-order total variation diminishing type Runge–Kutta method (Jiang & Shu 1996) is applied for time advancing.

https://doi.org/10.1017/jfm.2021.448 Published online by Cambridge University Press

Case	V_0	$X_{-4}V_2$	$X_{-4}V_4$	X_4V_2	X_4V_4
D_f	1.00	0.63	0.28	0.76	0.29

Table 5. Relative friction drag (the result of case V_0 is set to 1.00).

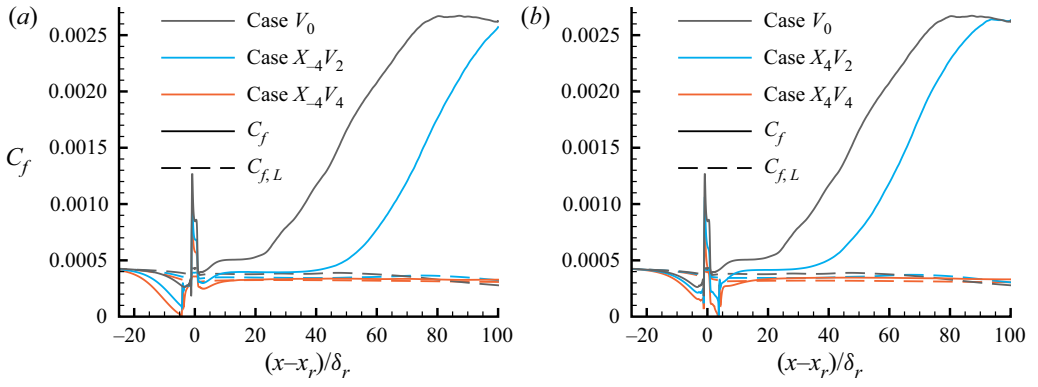


Figure 6. Spanwise-averaged $C_{f,x}$ and $C_{f,L}$ distributions of case V_0 and cases with blowing in (*a*) upstream position and (*b*) downstream position.

3. Results

First, the relative friction drag for the baseline case V_0 and cases with weak wall blowing ($I_{blow} \leq 0.04$) are demonstrated in table 5. It can be seen that both upstream and downstream-positioned blowing show a significant effect of reducing skin friction. In addition, the effect is remarkably enhanced with the increase in I_{blow}.

To further explore the role of wall blowing in the reduction of skin friction, a Fukagata–Iwamoto–Kasagi (FIK) decomposition (Fukagata, Iwamoto & Kasagi 2002) is conducted for these cases. For the plane compressible boundary layer with a zero pressure gradient, the skin friction can be decomposed into five components: laminar, turbulent, compressible, compressible–turbulent interaction and spatial development contributions (Gomez, Flutet & Sagaut 2009). The formula can be written as

$$C_f = \underbrace{\frac{4}{Re_\delta}\int_0^1 \overline{\rho_* u_*}\,\mathrm{d}y_*}_{C_{f,L}} + \underbrace{4\int_0^1 (1-y_*)\overline{\rho_* u_*'' v_*''}\,\mathrm{d}y_*}_{C_{f,T}} + C_{f,C} + C_{f,CT} + C_{f,D}, \tag{3.1}$$

where the boundary layer thickness Reynolds number $Re_\delta = \rho_\infty u_\infty \delta/\mu_w$ (with δ the local boundary layer thickness), q_* represents the non-dimensional value of quantity q based on ρ_∞, u_∞, T_w and δ, and q'' is the fluctuation value of quantity q based on Favre averaging.

For cases in this study, $C_{f,L}$ and $C_{f,T}$ are the two main components of C_f, so their results are reported in figures 6 and 7. As shown in figure 6, the gap between the distributions of $C_{f,L}$ in these cases is small. Therefore, the main contribution to the reduction of the friction drag force should be the turbulent contribution $C_{f,T}$.

The presumption above can be confirmed with the distributions of $C_{f,T}$ drawn in figure 7. In case V_0, behind the roughness element, a wake region is formed where the velocity fluctuation grows much more rapidly than in other regions. Then, it develops

https://doi.org/10.1017/jfm.2021.448 Published online by Cambridge University Press

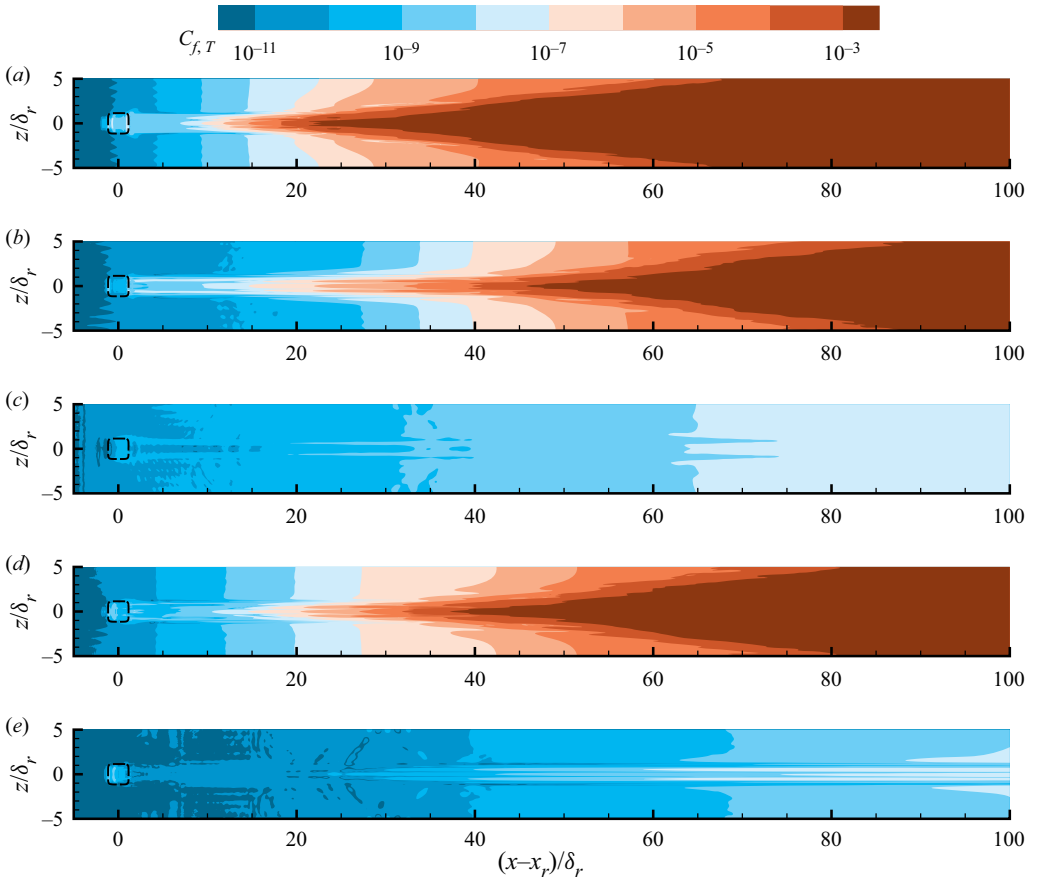


Figure 7. The $C_{f,T}$ distributions of (*a*) case V_0, (*b*) case $X_{-4}V_2$, (*c*) case $X_{-4}V_4$, (*d*) case X_4V_2 and (*e*) case X_4V_4. (The dashed line indicates the roughness shape at the height of $k_r/2$.)

into a turbulent wedge downstream and continuously broadens in the spanwise direction. Figure 7(*b–e*) shows that both upstream- and downstream-positioned blowing are able to significantly inhibit the transition process. For both cases in which $I_{blow} = 0.02$, the formation of a turbulent wedge is largely delayed. Moreover, the transition induced by the roughness element entirely disappears when the value of I_{blow} continues to increase. In conclusion, both upstream- and downstream-positioned blowing is able to reduce skin friction by inhibiting the roughness-induced transition.

In order to investigate the role of wall blowing in transition delay, it is necessary to clarify the mechanism of transition induced by smooth-edged roughness element in case V_0.

3.1. *Smooth-edged roughness-induced transition*

According to Subbareddy *et al.* (2014), typical structures in high-speed flow past a roughness element consist of (1) a horseshoe vortex system formed in the upstream separation zone, (2) an upstream shockwave system and (3) a separated shear layer/counter-rotating vortex system. These structures in case V_0 are visualized in figure 8.

https://doi.org/10.1017/jfm.2021.448 Published online by Cambridge University Press

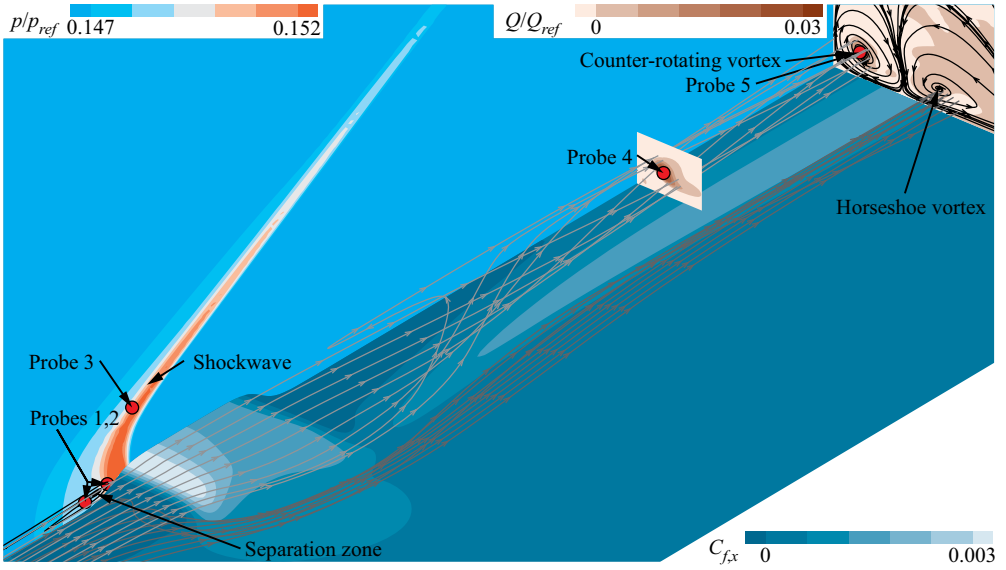


Figure 8. Visualization of the flow field, consisting of streamlines passing through the line $(x - x_r = -50\delta_r,\ y = 0.1\delta_r)$ (dark grey) or the line $(x - x_r = -50\delta_r,\ y = 0.2\delta_r)$ (light grey), streamlines on the symmetry plane and a slice $x - x_r = 10\delta_r$ (black), streamwise skin friction coefficient contour on the wall, non-dimensional pressure contour on the symmetry plane and non-dimensional Q criterion contours on slices $x - x_r = 7\delta_r$ and $x - x_r = 10\delta_r$ (here $p_{ref} = \gamma Ma_\infty^2$ and $Q_{ref} = u_\infty^2/\delta_r^2$).

The Q criterion in this figure is the second invariant of $\nabla \boldsymbol{u}$ (Hunt, Wray & Moin 1988):

$$Q = -\frac{1}{2}\left[\left(\frac{\partial u}{\partial x}\right)^2 + \left(\frac{\partial v}{\partial y}\right)^2 + \left(\frac{\partial w}{\partial z}\right)^2\right] - \frac{\partial u}{\partial y}\frac{\partial v}{\partial x} - \frac{\partial u}{\partial z}\frac{\partial w}{\partial x} - \frac{\partial v}{\partial z}\frac{\partial w}{\partial y}. \tag{3.2}$$

To determine which structure is the main source of unsteadiness in the transition process, five probes are adopted in the flow field (see figure 8) to record the fluctuation of pressure. Probes 1 and 2 are placed in the upstream separation zone, probe 3 is located at the shockwave, and probes 4 and 5 are in the counter-rotating vortex structure at $x - x_r = 7\delta_r$ or $x - x_r = 10\delta_r$. The power spectral density (PSD) of the pressure fluctuations at these probes is drawn in figure 9. The PSD spectrum is estimated using a fast Fourier transform (FFT) with uniform window. The sampling frequency is $St_{PSD} = 192.31$ (where St is the Strouhal number based on δ_r and u_∞), and 10 000 steps are recorded for each probe. The results show that the pressure fluctuations at the upstream separation region and the shockwave have the same dominant frequency (named mode 2). However, mode 2 disappears in the downstream region. At probes 4 and 5, the features of the dominant mode (named mode 1) are totally different from those of mode 2. The frequency of mode 1 is $St_1 = 0.422$ and that of mode 2 is $St_2 = 4.21$. The Strouhal number of mode 1 based on u_k and δ_r^* (displacement thickness at x_r) is $St_{k,1} = 0.309$, which is in the frequency range $0.2 \leq St_k \leq 0.5$ given by Klebanoff, Cleveland & Tidstrom (1992). Moreover, the frequency range of mode 1 is much wider than that of mode 2 in the spectrum. Recent studies of roughness-induced transition in the incompressible regime have shown that the dominant unsteadiness in the flow field results from the distorted wake structure downstream of the roughness (Loiseau *et al.* 2014; Citro *et al.* 2015; Bucci *et al.* 2018; Puckert & Rist 2018, 2019). Therefore, we can assume that the unsteadiness in the

https://doi.org/10.1017/jfm.2021.448 Published online by Cambridge University Press

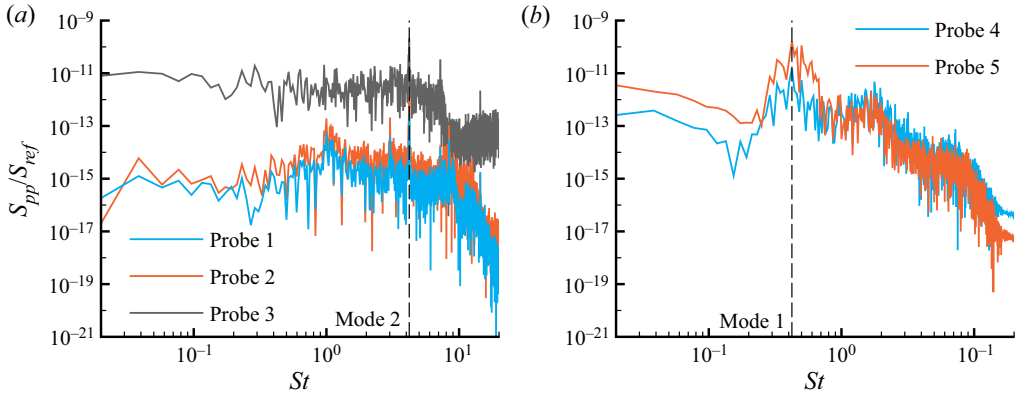


Figure 9. PSD results of pressure fluctuations at (*a*) probes 1–3 and (*b*) probes 4–5 (here $S_{ref} = p_{ref}^2 \delta_r / u_\infty$).

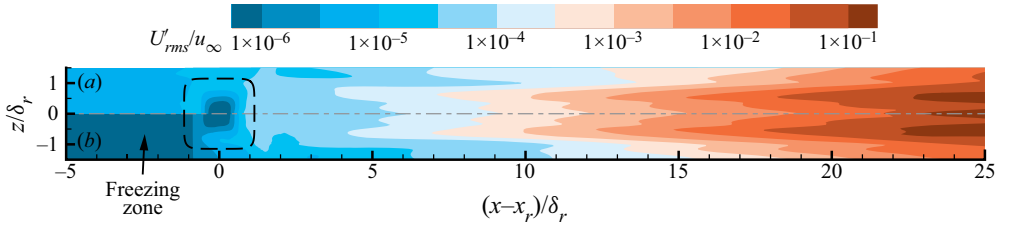


Figure 10. Comparison of non-dimensional velocity fluctuation distributions on the plane $y = k_r$ between (*a*) case V_0 and (*b*) case V_0 with a flow freezing operation. (The dashed line indicates the roughness shape at the height of $k_r/2$.)

roughness-induced transition process of case V_0 mainly comes from the separated shear layer/counter-rotating vortex system in the downstream region of roughness.

To confirm the assumption, we perform a flow freezing operation (Shrestha & Candler 2019). In this operation, the conservative variables $\boldsymbol{Q}$ in the freezing zone are fixed at average value. Flow in the upstream region of the roughness element is frozen so that the upstream separation zone and the shockwave can contribute little to the unsteadiness in the downstream region. However, it can be observed from figure 10 that the freezing of the upstream flow rarely affects the development of disturbance. This proves that the main unsteadiness in the roughness-induced transition process originates from the downstream region.

Additionally, three-dimensional spectral proper orthogonal decomposition (SPOD) (Lumley 1970) and DMD (Rowley *et al.* 2009; Schmid 2010) of the near-roughness region ($-2.75\delta_r \leq x - x_r \leq 12.75\delta_r$, $y \leq 1.25\delta_r$ and $-2.5\delta_r \leq z \leq 2.5\delta_r$) are conducted to support the findings above. The total number of grid points is approximately 1.5 million, and 500 snapshots are recorded for our study. The sampling frequency is $St_{SPOD} = St_{DMD} = 38.46$. For SPOD, the number of snapshots in each block is $N_f = 250$, and the number of overlap snapshots is $N_o = 225$. An identity matrix is used as the weight matrix. The code we use for SPOD is provided by Towne, Schmidt & Colonius (2018). The SPOD results are consistent with the PSD analysis above. The peak of mode 2 appears clearly in the SPOD spectra for the upstream region of roughness ($x - x_r \leq -0.85\delta_r$) (see figure 11*a*), and almost disappears in the results of the whole near-roughness region (see figure 11*b*). The dominant mode in the spectra of near-roughness region is mode 1.

https://doi.org/10.1017/jfm.2021.448 Published online by Cambridge University Press

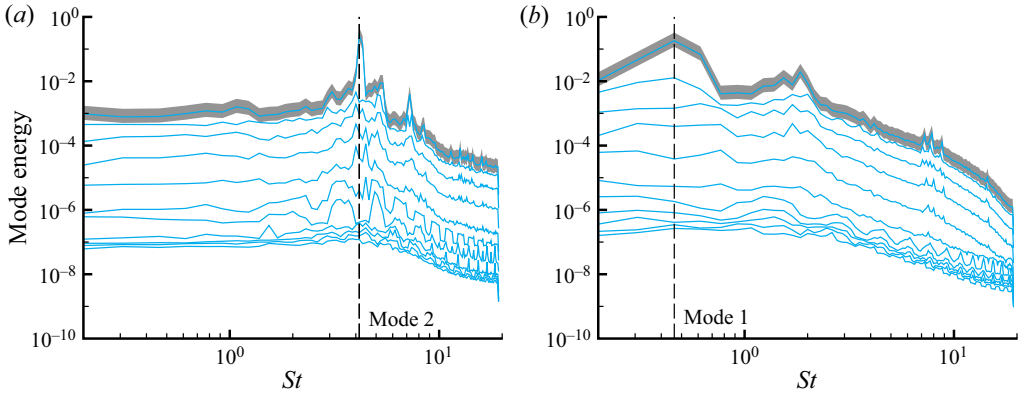


Figure 11. SPOD results of (*a*) the upstream region ($-2.75\delta_r \leq x - x_r \leq -0.85\delta_r$, $y \leq 1.25\delta_r$ and $-2.5\delta_r \leq z \leq 2.5\delta_r$) and (*b*) the whole near-roughness region ($-2.75\delta_r \leq x - x_r \leq 12.75\delta_r$, $y \leq 1.25\delta_r$ and $-2.5\delta_r \leq z \leq 2.5\delta_r$) of case V_0. (The grey areas are the 99 % confidence interval.)

The algorithm for DMD employed in this paper comes from Sayadi & Schmid (2016), and sparsity-promoting DMD (DMDSP) (Jovanović, Schmid & Nichols 2014) is also used here to select the dominant DMD modes. From the distribution of eigenvalues shown in figure 12(*a*), we can see that most of the modes are on the unit circle, which indicates that the development of the flow field is saturated (Subbareddy *et al.* 2014). Both the upstream and downstream dominant modes can be picked out by DMDSP with different parameters, and the results reveal that mode 1 is much more dominant than mode 2. Figure 12(*b*) demonstrates the pressure fluctuation of mode 1 extracted by DMD analysis, and figure 12(*c*) is the distribution of the shear layer separated from the roughness element. The shear layer is indicated by local shear u_s (Shrestha & Candler 2019):

$$u_s = \sqrt{\left(\frac{\partial u}{\partial y}\right)^2 + \left(\frac{\partial u}{\partial z}\right)^2}. \tag{3.3}$$

The fluctuation growth of unstable mode 1 is mainly in the downstream region of the roughness, and the position where the amplitude of fluctuation increases most rapidly is close to the shear layer. This is consistent with our supposition above that the main source of unsteadiness in the transition process is the separated shear layer/counter-rotating vortex system in the wake structure. Besides, the pressure fluctuations of mode 1 at $x - x_r = 11.5\delta_r$ and $x - x_r = 12.5\delta_r$ show axial symmetry, and the maximum value of fluctuation is situated along the symmetry axis (see figure 12*d*,*e*). This agrees with the feature of a varicose mode, which exists due to the instability of the shear layer induced by the counter-rotating vortex pair in the wake (De Tullio *et al.* 2013).

To further demonstrate the relationship between the separated shear layer/counter-rotating vortex system and the development of disturbances, several slices of the flow field for case V_0 are drawn in figure 13. In figure 13(*a*) we can clearly observe that the horseshoe vortex and the counter-rotating vortex pair trail downstream behind the roughness, and the separated shear layer forms over the counter-rotating vortex. The in-plane streamlines illustrate a heavy distortion of the boundary layer caused by the streamwise vortices in the wake structure. With the flow going downstream, all the streamwise vortices in the wake are dissipated, and the distortion is relaxed. However, the separated shear layer is bent by the counter-rotating vortex pair and gradually wraps around it. The interaction of the separated shear layer/counter-rotating vortex system maintains the strength of the

https://doi.org/10.1017/jfm.2021.448 Published online by Cambridge University Press

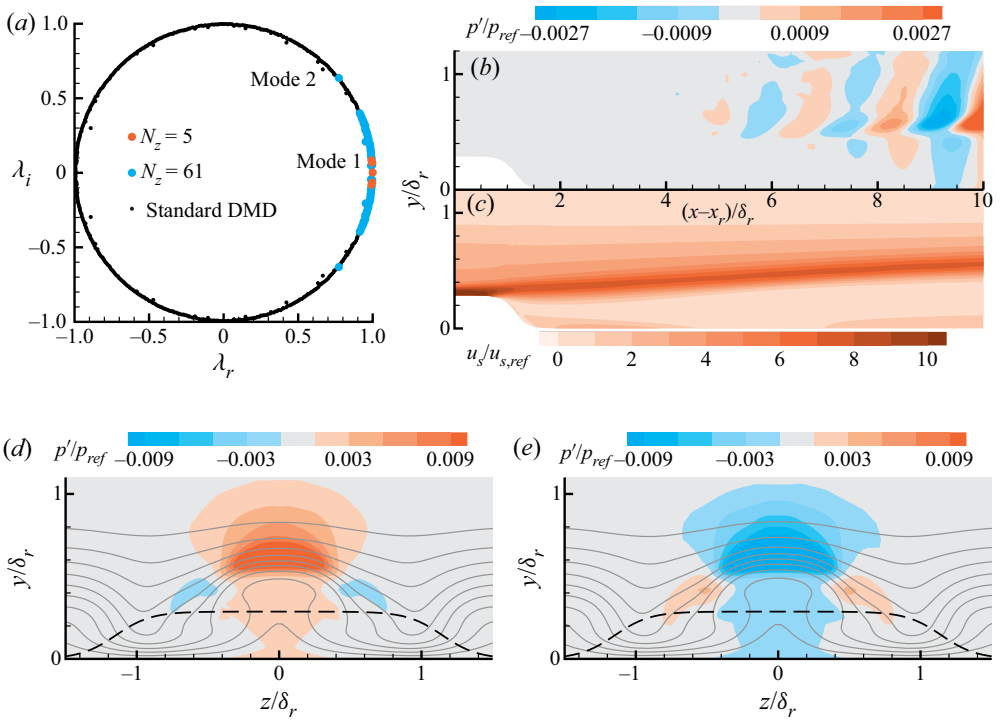


Figure 12. DMD results of case V_0: (*a*) eigenvalues from standard DMD and DMDSP with N_z DMD modes; (*b*) reconstruction of mode 1 extracted by DMD; (*c*) the distribution of streamwise shear on the symmetry plane ($u_{s,ref} = u_\infty/\delta_r$); and reconstruction of mode 1 at (*d*) $x - x_r = 11.5\delta_r$ and (*e*) $x - x_r = 12.5\delta_r$. (The grey solid lines in panels (*d*,*e*) are isolines of u with the same value set, and the black dashed line indicates the projection of roughness.)

shear layer and induces a rapid disturbance growth at its position (see figure 13*b*,*d*,*f*). In addition, the lift-up effect (Landahl 1980; Brandt 2014) caused by the streamwise counter-rotating vortex not only induces disturbance transient growth (Reshotko 2001) but more importantly amplifies the interaction, which is also observed by Shrestha & Candler (2019).

3.2. *Weak wall blowing inhibiting transition*

With the understanding of the smooth-edged roughness-induced transition in § 3.1, we can now look into the mechanism of two-dimensional upstream-/downstream-positioned weak wall blowing inhibiting transition.

For the two cases with upstream-positioned weak blowing $X_{-4}V_2$ and $X_{-4}V_4$, the same three slices of the flow field are plotted in figure 14 as a comparison with case V_0. It is obvious that the configuration of the wake structure changes little at $x - x_r = 6\delta_r$ between cases with or without upstream-positioned blowing. Only the strength of those main structures in the wake is diminished and the distortion of the boundary layer profile is reduced. As a result, the interaction between the separated shear layer and counter-rotating vortex is inhibited, and the shear layer is not as bent as in case V_0 and is also relaxed along the streamwise direction, especially in case $X_{-4}V_4$. Therefore, the disturbance growth rate is decreased. As roughness-induced transition is a competitive mechanism between the development of unsteady fluctuation and the relaxation of the wake structure

https://doi.org/10.1017/jfm.2021.448 Published online by Cambridge University Press

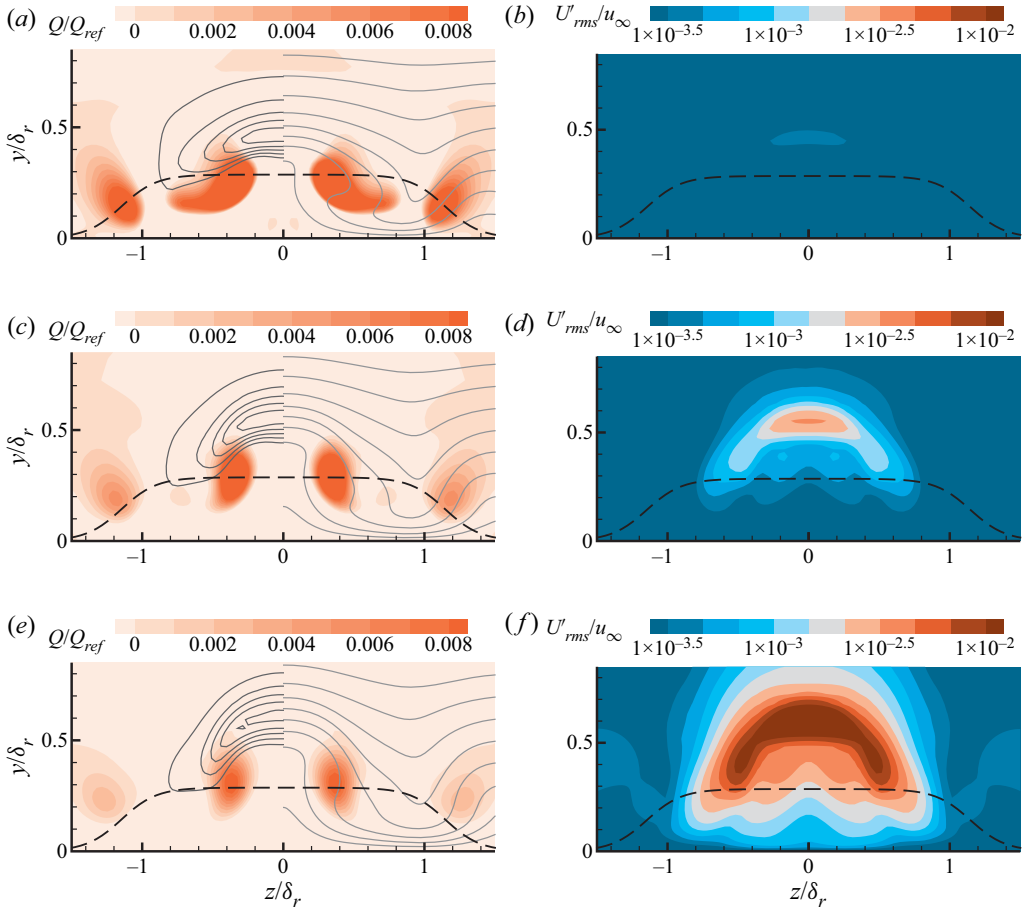


Figure 13. Slices of case V_0 at (*a*,*b*) $x - x_r = 6\delta_r$, (*c*,*d*) $x - x_r = 10\delta_r$ and (*e*,*f*) $x - x_r = 14\delta_r$ coloured with (*a*,*c*,*e*) non-dimensional Q criterion and (*b*,*d*,*f*) streamwise velocity fluctuation. (The dark grey solid lines on the left half of (*a*,*c*,*e*) are isolines of u_s with the same value set; the light grey lines on the right are in-plane vortex lines; and the black dashed line indicates the projection of roughness.)

(Ergin & White 2006), the transition process in both cases with upstream blowing position is delayed, as shown in figure 7.

It is actually easy to understand the mechanism of the wake structure being weakened by upstream-positioned blowing. The upstream-positioned blowing does not directly interact with the wake structure. Instead, the comparison of the boundary layer profile on the symmetry plane between cases V_0 and $X_{-4}V_4$ drawn in figure 15 shows that the upstream-positioned blowing is able to lift the inflow boundary layer, which may result in a decrease in the effective value of Re_{kk}. Therefore, we conduct two-dimensional DNS computations of upstream-positioned weak wall blowing cases but without the roughness element, and the results are reported in table 6. From the results we can see that the upstream-positioned blowing greatly reduces the effective roughness Reynolds number Re^*_{kk}, which leads to the weakening of the wake structure. In addition, the zoomed-in boundary layer profile demonstrates that the upstream-positioned blowing also has the effect of moving the separation position backwards, which determines the structures of the horseshoe vortex system forming in the separation zone (Baker 1979).

https://doi.org/10.1017/jfm.2021.448 Published online by Cambridge University Press

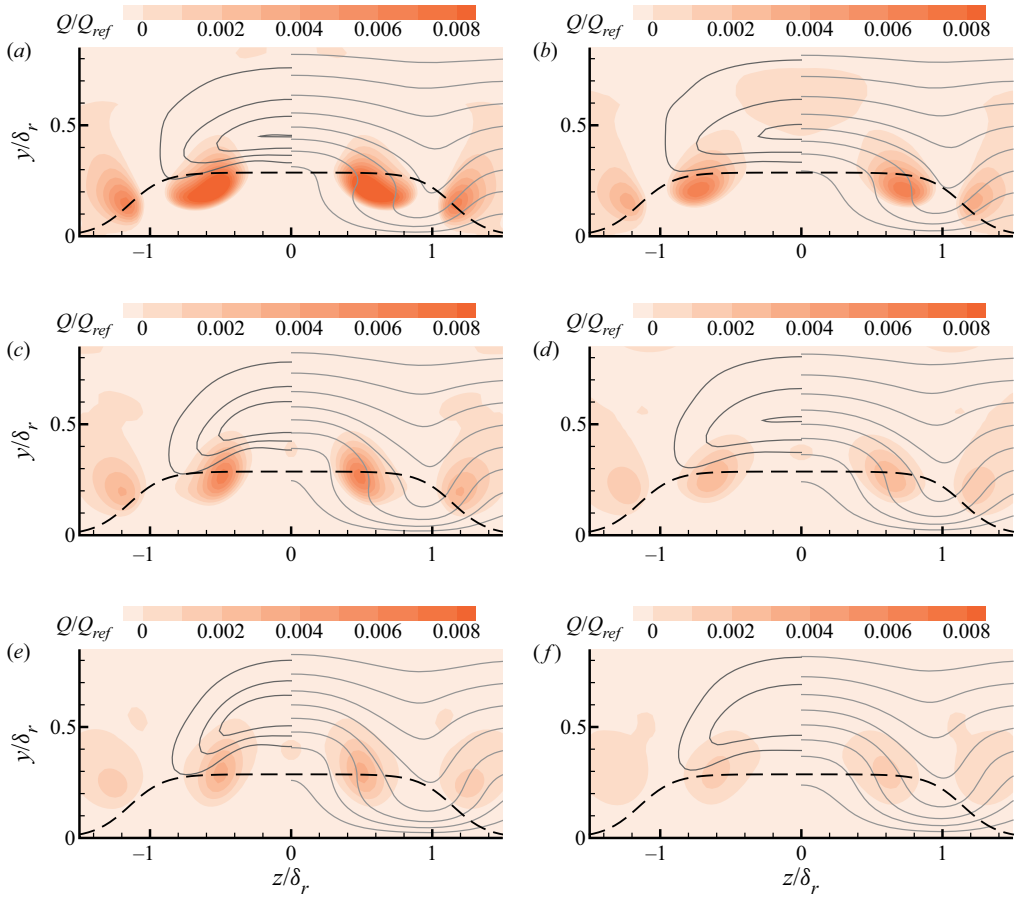


Figure 14. Slices of (*a*,*c*,*e*) case $X_{-4}V_2$ and (*b*,*d*,*f*) case $X_{-4}V_4$ at (*a*,*b*) $x - x_r = 6\delta_r$, (*c*, *d*) $x - x_r = 10\delta_r$ and (*e*,*f*) $x - x_r = 14\delta_r$ coloured with the non-dimensional Q criterion. (The dark grey solid lines on the left half are isolines of u_s with the same value set; the light grey lines on the right are in-plane vortex lines; and the black dashed line indicates the projection of roughness.)

Case	δ_r^*/δ_r	ρ_k/ρ_∞	u_k/u_∞	T_k/T_∞	Re_{kk}^*
V_0	1	0.562	0.379	1.78	420
$X_{-4}V_2$	1.06	0.549	0.309	1.81	329.94
$X_{-4}V_4$	1.12	0.541	0.255	1.84	265.71

Table 6. Effective roughness Reynolds number and inflow boundary layer parameters (here δ_r^* is the actual boundary layer thickness at the centre point of roughness).

The PSD results illustrated in figure 16 for both cases with upstream blowing position also support our analysis. Owing to the changes in vortex structures in the upstream separation zone shown in figure 15, the unstable mode 2 in the upstream region is weakened in case $X_{-4}V_2$ and disappears in case $X_{-4}V_4$. In the downstream region, the unstable mode 1 has the same varying tendency. The amplitudes of both modes are reduced by approximately an order of magnitude in case $X_{-4}V_2$ compared with case V_0.

https://doi.org/10.1017/jfm.2021.448 Published online by Cambridge University Press

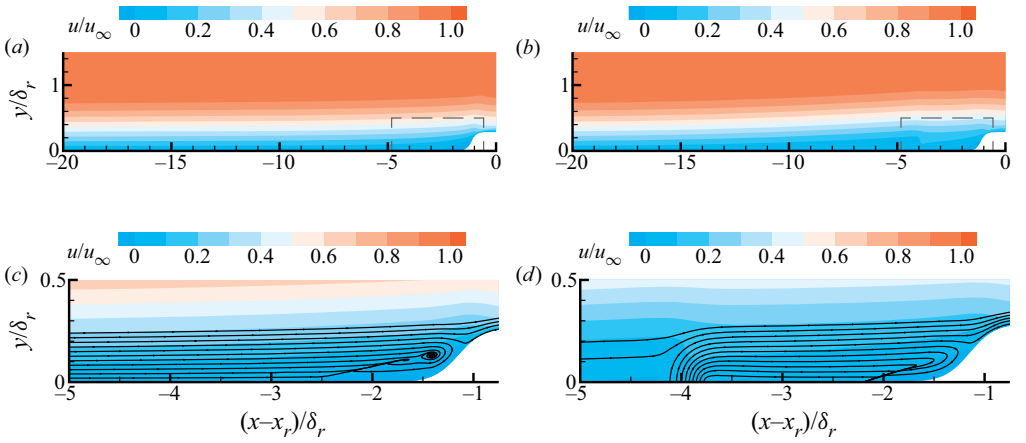


Figure 15. Profiles of non-dimensional streamwise velocity on the symmetry plane of (*a*,*c*) case V_0 and (*b*,*d*) case $X_{-4}V_4$. Panels (*c*,*d*) are zoomed-in views of the grey dashed rectangular regions in panels (*a*,*b*); black solid lines are in-plane streamlines.

Additionally, the frequency of mode 1 falls with the reduction of Re^*_{kk}, which agrees with the result reported by Klebanoff *et al.* (1992).

In regard to downstream blowing position, its effect is the delay of the roughness-induced transition through completely different mechanisms. The comparison between figures 17 and 15(*c*) shows that the downstream-positioned blowing has much less impact on the separation zone and horseshoe vortex system than the upstream-positioned blowing. This suggests that the contribution of downstream-positioned blowing in delaying the transition mainly comes from its direct interaction with the downstream wake structure.

The slices of case X_4V_2 at $x - x_r = 5\delta_r$ demonstrated in figure 18(*b*) indicate that the wake structure in the downstream region of cases with downstream blowing position is distinct from cases with upstream blowing position or without blowing, which is apparently due to the direct interaction between the wake structure and wall blowing. The main difference is that a new vortex pair is formed under the original counter-rotating vortex pair in case X_4V_2, and the rotation directions of these two vortex pairs are opposite. The original counter-rotating vortex pair is squeezed and pushed away from the wall in the wall-normal direction and stretched in the spanwise direction. The new vortex pair comes from the secondary vortex induced by the original counter-rotating vortex pair in the near-wall region due to the no-slip wall boundary condition. As illustrated in figure 18(*d*), the secondary vortex is lifted away from the wall by downstream-positioned wall blowing.

For a further exploration of wake structure development in cases with downstream blowing position, the same three slices of the boundary layer are drawn in figure 19. The results suggest that the weakening of the separated shear layer caused by the downstream-positioned blowing is not as effective as that due to upstream-positioned blowing with the same intensity. However, the downstream-positioned blowing is able to provide a similar effect to the upstream-positioned blowing on diminishing the magnitude of the counter-rotating vortex pair in the wake. Therefore, the shear layer/counter-rotating vortex interaction is weakened, and the shear layer is less bent than in case V_0. As a result, the disturbance development induced by the interaction is inhibited and the transition is delayed as displayed in figure 7. In summary, the downstream-positioned blowing takes

https://doi.org/10.1017/jfm.2021.448 Published online by Cambridge University Press

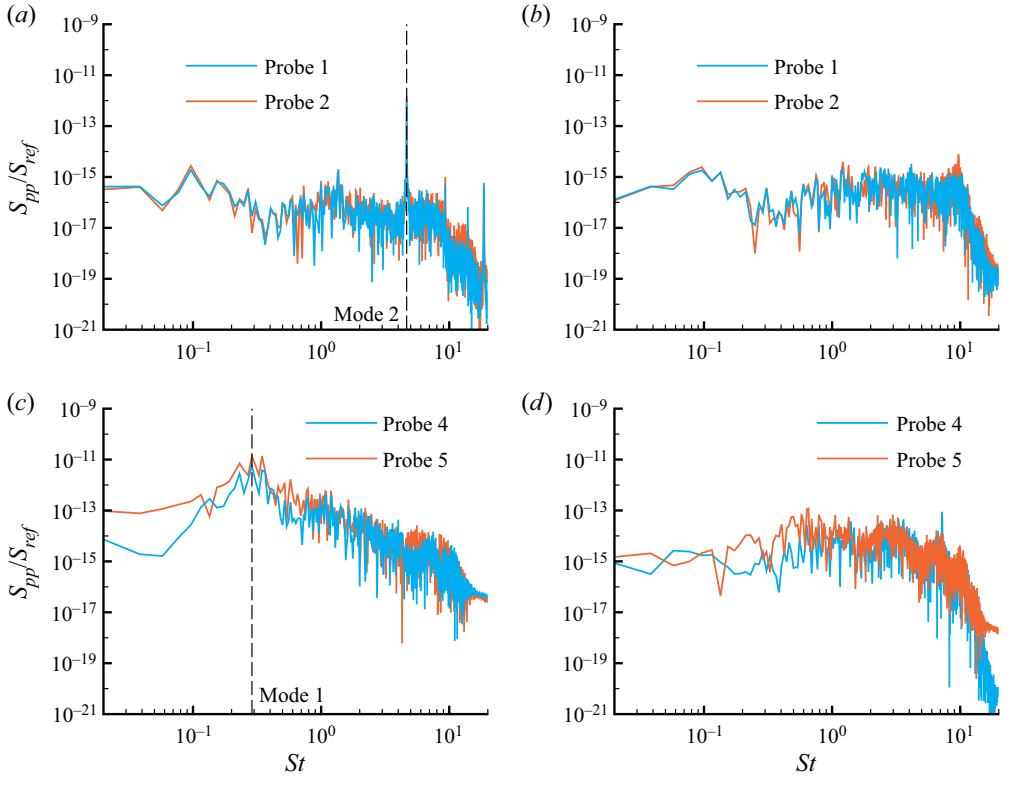


Figure 16. PSD results of (*a*,*c*) case $X_{-4}V_2$ and (*b*,*d*) case $X_{-4}V_4$ at the (*a*,*b*) upstream region and (*c*,*d*) downstream region.

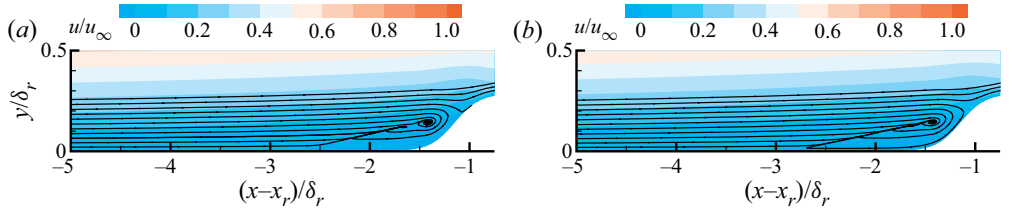


Figure 17. Profiles of the non-dimensional streamwise velocity on the symmetry plane of (*a*) case X_4V_2 and (*b*) case X_4V_4. (Black solid lines are in-plane streamlines.)

effect on delaying the roughness-induced transition by rapidly diminishing the magnitude of the counter-rotating vortex pair in the wake structure.

Two possible approaches are proposed here to explain the weakening of the counter-rotating vortex pair: the downstream-positioned blowing can provide much stronger dissipation for streamwise vortices, and the two-dimensional wall blowing is able to convert some streamwise vorticities into spanwise types. To confirm our supposition, vorticity transportation analysis is employed. For quantity $\omega_i^2/2$ (where ω_i represents the angular velocity component in direction i), its transportation equation can be written as (Brown, Lee & Moser 2015; Suryanarayanan *et al.* 2020):

https://doi.org/10.1017/jfm.2021.448 Published online by Cambridge University Press

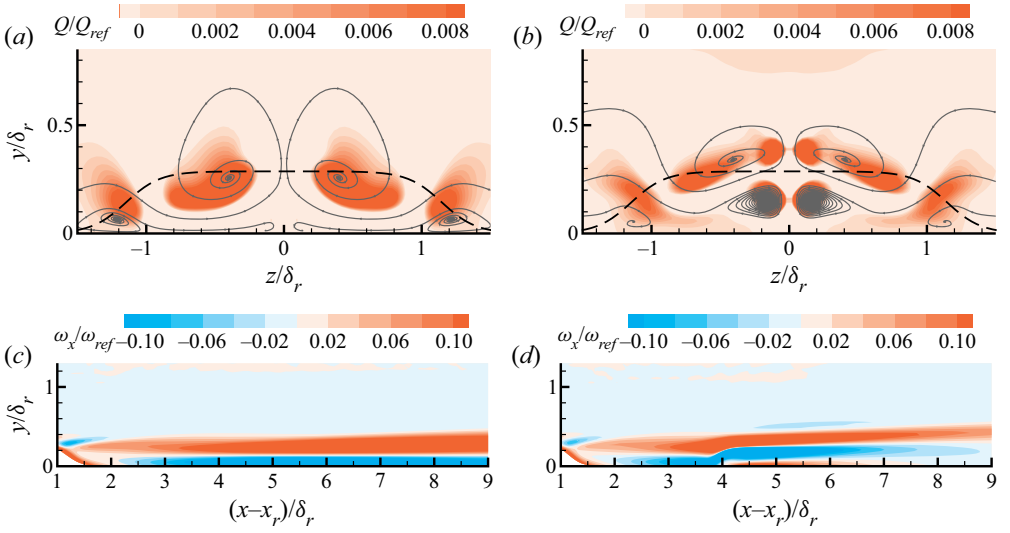


Figure 18. Comparison of wake structures between (*a*,*c*) case V_0 and (*b*,*d*) case X_4V_2: (*a*,*b*) slices of the non-dimensional Q criterion at $x - x_r = 5\delta_r$ and (*c*,*d*) non-dimensional streamwise angular velocity profiles at $z = 0.3\delta_r$. (The grey solid lines are in-plane streamlines, and the black dashed line indicates the projection of roughness, $\omega_{ref} = u_\infty/\delta_r$.)

$$\frac{\partial}{\partial t}\left(\frac{1}{2}\omega_i^2\right) + \boldsymbol{u}\cdot\nabla\left(\frac{1}{2}\omega_i^2\right) = \omega_i\boldsymbol{\omega}\cdot\nabla u_i + \nu[\nabla^2\left(\frac{1}{2}\omega_i^2\right) - |\nabla\omega_i|^2], \tag{3.4}$$

where $\boldsymbol{\omega}$ is the angular velocity vector. In this equation, the dissipation term is $D_i = \nu|\nabla\omega_i|^2$, and the source term is $S_i = \omega_i\,\boldsymbol{\omega}\cdot\nabla u_i = \sum_j S_{ij}$. The component of the source term $S_{ii} = \omega_i^2\,\partial u_i/\partial x_i$ represents the stretch of ω_i, and component $S_{ij} = \omega_i\omega_j\,\partial u_i/\partial x_j$ denotes the conversion from ω_j to ω_i.

Profiles of the vortex transportation are plotted in figure 20 to verify the first approach. It can be observed in figure 20(*b*) that the counter-rotating vortex experiences a short period of increase upstream of the blowing slot. This results from the stretch of ω_x induced by wall blowing (see the peak value of S_{xx} in figure 20*d*). Meanwhile, as demonstrated in figure 18(*d*), the wall blowing can also lift the counter-rotating vortex pair and its secondary vortex and squeeze the space between them. Both enlarging the magnitude of the streamwise vortex and squeezing them in the wall-normal direction are able to increase the gradient of ω_x and consequently provide a much stronger dissipation than in case V_0 (see figure 20*e*,*f*).

Similarly, the second approach can be proven by comparing the profiles of source term S_{zx} drawn in figure 21. In figure 21(*b*), an obvious peak region can be observed over the blowing slot located at $x_{blow} - x_r = 4\delta_r$. The peak value of S_{zx} indicates a strong conversion from the streamwise vorticity to the spanwise type, which also contributes to the weakening of the counter-rotating vortex pair.

PSD analyses are also conducted for these two cases with downstream-positioned weak wall blowing, and their results shown in figure 22 agree well with our analysis above. As the downstream-positioned blowing has little influence on the upstream region, which is shown in figure 17, the unstable mode 2 always exists, even in case X_4V_4, where the transition does not occur downstream. However, for the downstream region, the dominant mode 1 only exists in case X_4V_2, and its amplitude is decreased compared to case V_0.

https://doi.org/10.1017/jfm.2021.448 Published online by Cambridge University Press

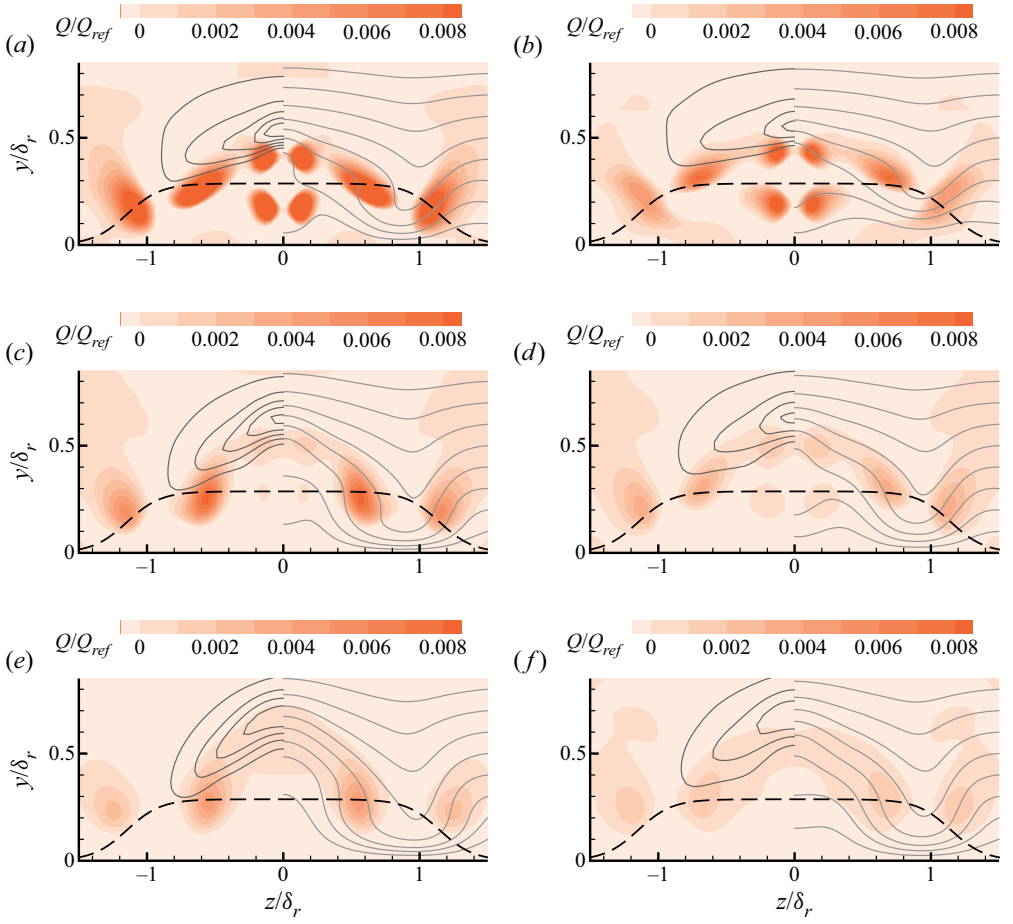


Figure 19. Slices of (*a*,*c*,*e*) case X_4V_2 and (*b*,*d*,*f*) case X_4V_4 at (*a*,*b*) $x - x_r = 6\delta_r$, (*c*,*d*) $x - x_r = 10\delta_r$ and (*e*,*f*) $x - x_r = 14\delta_r$ coloured with the non-dimensional Q criterion. (The dark grey solid lines on the left half are isolines of u_s with the same value set; the light grey lines on the right are in-plane vortex lines; and the black dashed line indicates the projection of roughness.)

Moreover, as the effect of downstream-positioned blowing on reducing Re^*_{kk} is not as great as the upstream one, the frequency of mode 1 in case X_4V_2 is between case V_0 and case $X_{-4}V_2$.

3.3. *Strong wall blowing promoting transition*

According to the results demonstrated in table 5, the skin friction decreases with increasing I_{blow} for both upstream- and downstream-positioned weak wall blowing. However, this trend cannot always continue. The results reported in table 7 indicate that, in cases with strong wall blowing, the increase in I_{blow} leads to a significant growth in the friction drag force.

Experimental (Bajura & Catalano 1975), theoretical (Tsuji *et al.* 1977) and numerical (Wernz & Fasel 1997) studies have shown that two-dimensional wall blowing with overstrength can introduce unsteadiness into the flow field and lead to transitions downstream. Similar results are also observed in this study. From figure 23, we can see

https://doi.org/10.1017/jfm.2021.448 Published online by Cambridge University Press

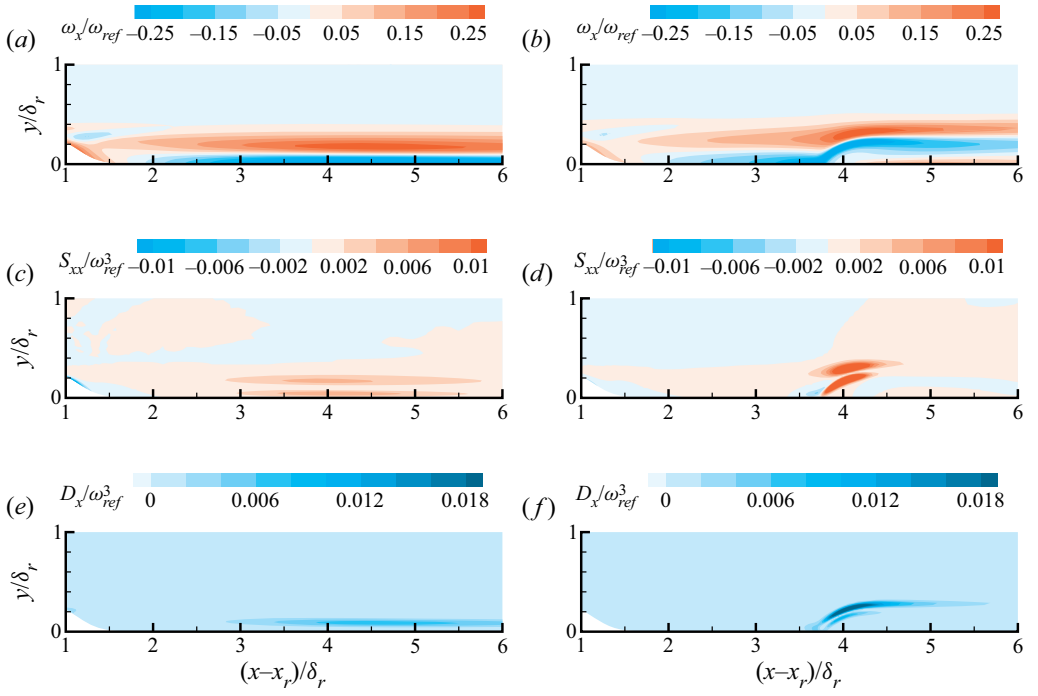


Figure 20. Profiles of (*a*,*c*,*e*) case V_0 and (*b*,*d*,*f*) case X_4V_4 at $z = 0.5\delta_r$ coloured with (*a*,*b*) the non-dimensional streamwise angular velocity, (*c*,*d*) vorticity transportation term S_{xx} and (*e*,*f*) D_x.

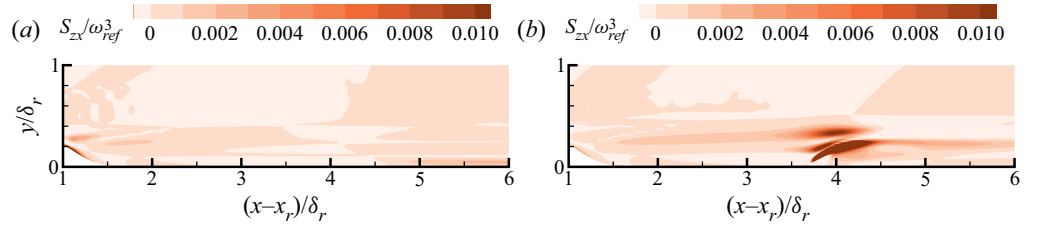


Figure 21. Profiles of (*a*) case V_0 and (*b*) case X_4V_4 at $z = 0.5\delta_r$ coloured with the non-dimensional vorticity transportation term S_{zx}.

Case	V_0	$X_{-4}V_{18}$	$X_{-4}V_{20}$	X_4V_{23}	X_4V_{25}
D_f	1.00	0.15	0.80	0.16	0.76

Table 7. Relative friction drag (the result of case V_0 is set to 1.00).

that, in contrast to weak wall blowing cases, flow in the wake remains laminar when I_{blow} is small (cases $X_{-4}V_{18}$ and X_4V_{23}), and breaks down into turbulence in cases with stronger blowing (cases $X_{-4}V_{20}$ and X_4V_{25}).

For the two cases with upstream-positioned strong wall blowing, slices at $x - x_r = 6$ are drawn in figure 24. It can be observed that the separated shear layer in both cases is very weak compared to other cases in this paper, and this can be attributed to the much smaller

https://doi.org/10.1017/jfm.2021.448 Published online by Cambridge University Press

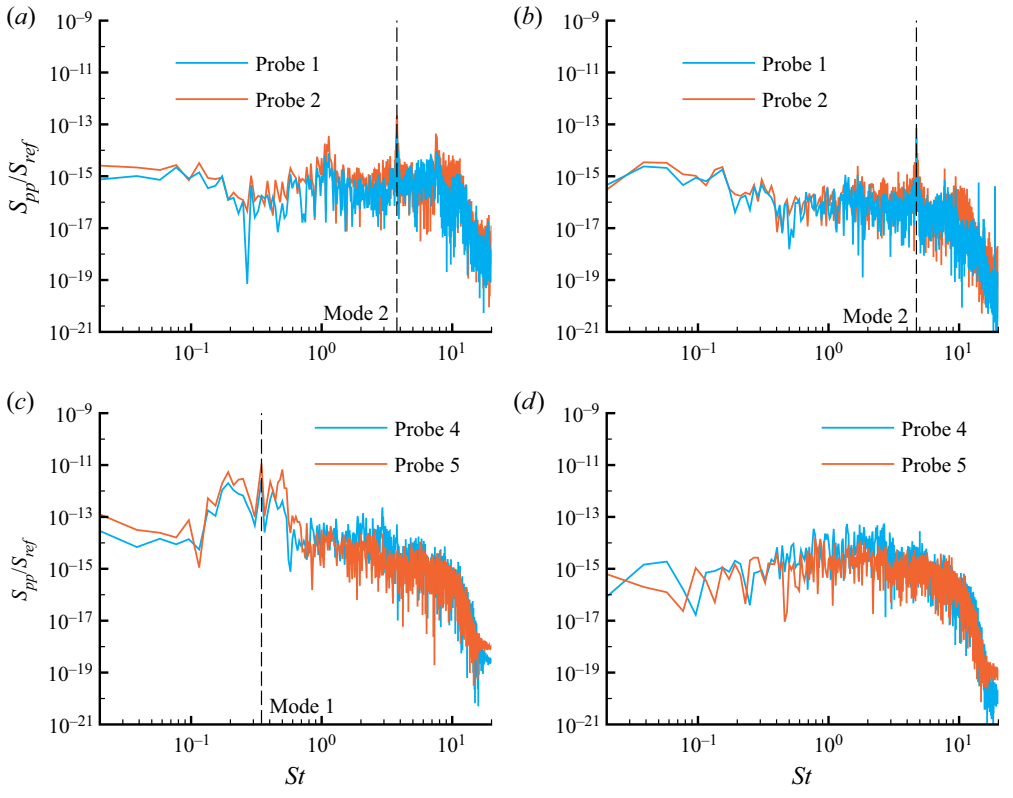


Figure 22. PSD results of (*a*,*c*) case X_4V_2 and (*b*,*d*) case X_4V_4 at the (*a*,*b*) upstream region and (*c*,*d*) downstream region.

effective roughness Reynolds number. The value of Re^*_{kk} for case $X_{-4}V_{18}$ is 113.57, and for case $X_{-4}V_{20}$ is 72.11. However, with the value of I_{blow} increasing from 0.18 to 0.20, the wake structure experiences a substantial change. The in-plane streamlines in figure 24(*a*) illustrate that the difference of wake structures between case $X_{-4}V_{18}$ and case V_0 is small, but the streamwise vortices in the boundary layer of case $X_{-4}V_{20}$ become stronger and form much more complicated flow structures. This is because the wake in case $X_{-4}V_{20}$ soon becomes unstable and induces a much stronger disturbance than that in $X_{-4}V_{18}$ (see figure 24*d*).

For exploring the source of unsteadiness, the time sequence of pressure fluctuation p' at the upstream region (probes 1 and 2) and $x - x_r = 6\delta_r$ (probe 6 in figure 24) are recorded for PSD analysis. Owing to the upstream-positioned strong blowing, there exists a strong unstable mode 2 in the upstream separation zone (see figure 25*a*). (The peak of the PSD spectrum at $St \approx 15$ is a harmonic of mode 2.) However, mode 2 still cannot induce a transition downstream. Meanwhile, a new unstable mode appears in the PSD results of case $X_{-4}V_{20}$, and it is marked as mode 3. The amplitude of mode 3 is more than one order of magnitude larger than that of mode 2 in figure 25(*b*), and its frequency is between those of mode 1 and mode 2. More importantly, unlike mode 2, the unstable mode 3 maintains its amplitude in the propagation towards the downstream region. Meanwhile, there exists the unstable mode 1 downstream, which is the dominant mode in the transition process of cases with weak wall blowing or without it. With the findings above, we suppose that

https://doi.org/10.1017/jfm.2021.448 Published online by Cambridge University Press

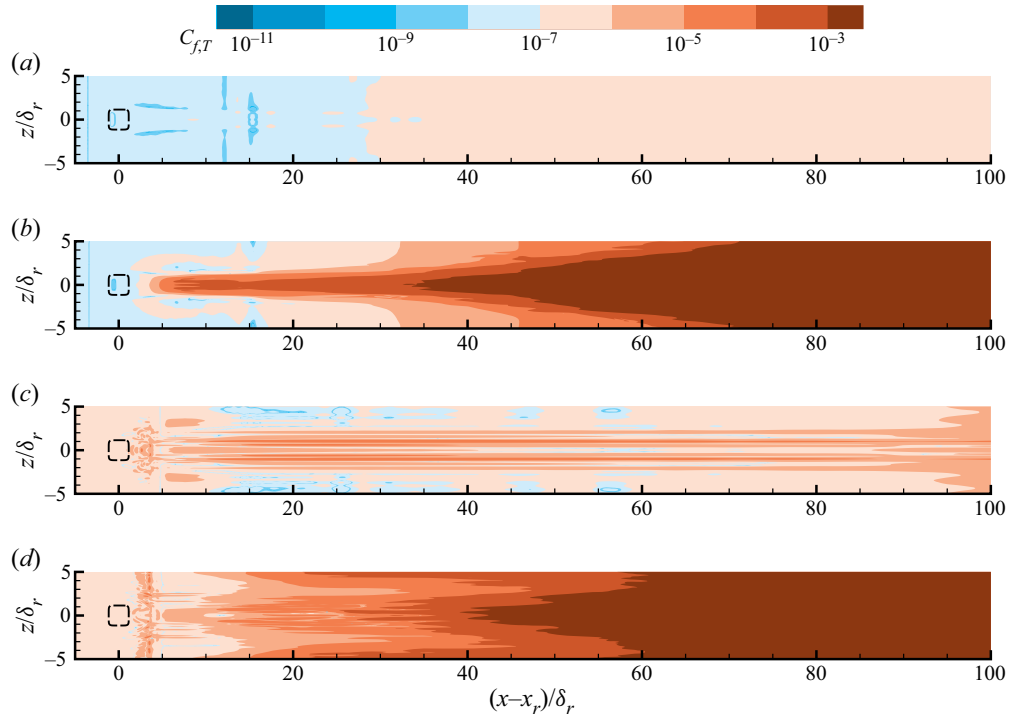


Figure 23. The $C_{f,T}$ distributions of (*a*) case $X_{-4}V_{18}$, (*b*) case $X_{-4}V_{20}$, (*c*) case X_4V_{23} and (*d*) case X_4V_{25}. (The dashed line indicates the roughness shape at the height of $k_r/2$.)

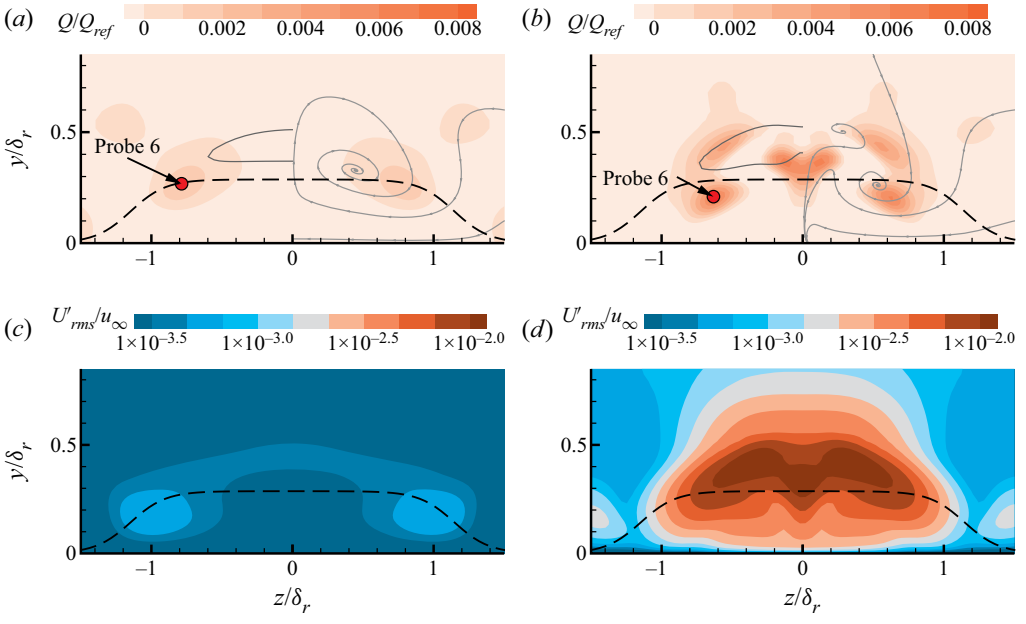


Figure 24. Slices of (*a*,*c*) case $X_{-4}V_{18}$ or (*b*,*d*) case $X_{-4}V_{20}$ at $x - x_r = 6\delta_r$ coloured with (*a*,*b*) the non-dimensional Q criterion and (*c*,*d*) the streamwise velocity fluctuation. (The dark grey solid lines on the left half of (*a*,*b*) are isolines of u_s with the same value set; the light grey lines on the right are in-plane streamlines; and the black dashed line indicates the projection of roughness.)

https://doi.org/10.1017/jfm.2021.448 Published online by Cambridge University Press

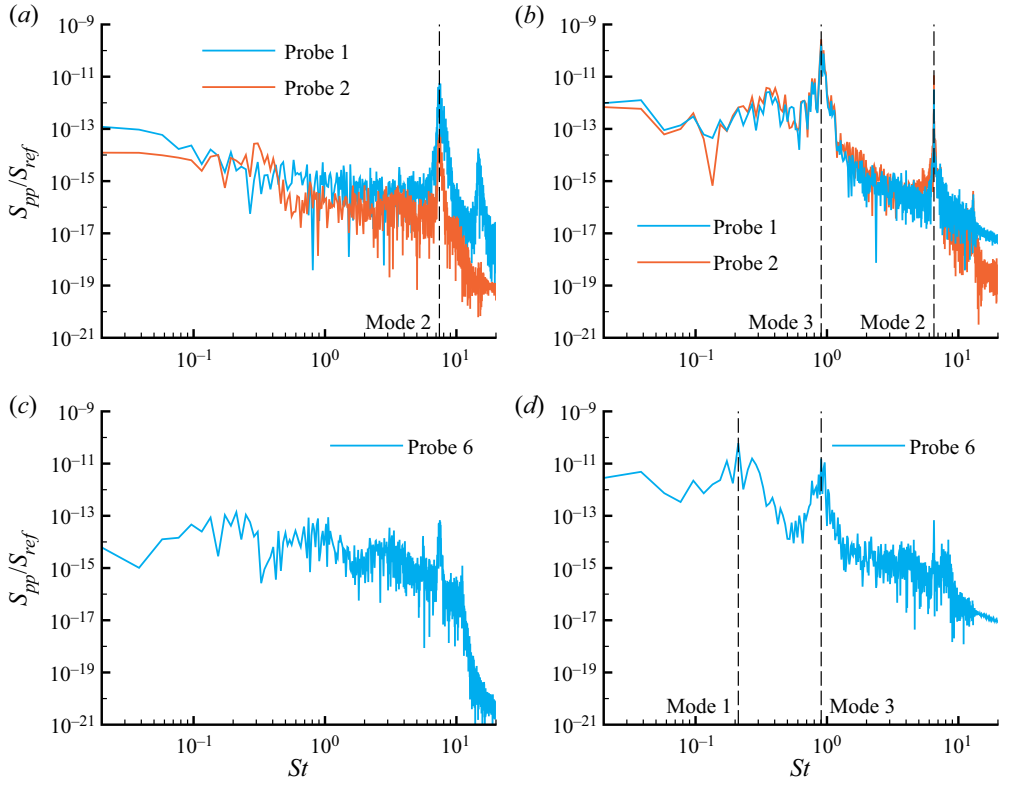


Figure 25. PSD results of (*a*,*c*) case $X_{-4}V_{18}$ and (*b*,*d*) case $X_{-4}V_{20}$ at (*a*,*b*) the upstream region and (*c*,*d*) $x - x_r = 6\delta_r$.

mode 1 in the downstream region of case $X_{-4}V_{20}$ is induced by mode 3, or mode 3 is the key factor for the transition process of cases with upstream-positioned strong wall blowing.

To determine the source of unstable mode 3, we re-examine the flow field of these two cases. As demonstrated in figure 26(*a*,*b*), a much larger separation zone forms upstream of the blowing slot, which could be the source of mode 3. Therefore, probes 7 and 8 are placed in this separation zone for PSD analysis, and the results of both cases are demonstrated in figure 26(*c*,*d*). The unstable mode 3 can be clearly observed at this separation zone in case $X_{-4}V_{20}$ as the only dominant frequency, while in case $X_{-4}V_{18}$, there is no obvious dominant unstable mode in this region.

Then, a flow freezing operation is conducted for the separation zone upstream of the blowing slot in case $X_{-4}V_{20}$ to confirm the role of unstable mode 3 in the transition process. From the comparison of velocity fluctuation development at $y = k_r$ illustrated in figure 27(*a*,*b*), we can see that, due to the freezing operation of the separation zone, the disturbance level near the region of the roughness element is diminished by approximately two orders of magnitude. Although the disturbance still grows in the near-wake region, the lower initial disturbance level results in a peak disturbance level that is not enough for breakdown into turbulence when the distortion of the boundary layer profile is relaxed. The PSD results in figure 27(*c*,*d*) also agree with our analysis above. As the separation zone located at the upstream side of the blowing slot is frozen, the unstable mode 3 disappears in the upstream region of the roughness element, and mode 2 becomes the only

https://doi.org/10.1017/jfm.2021.448 Published online by Cambridge University Press

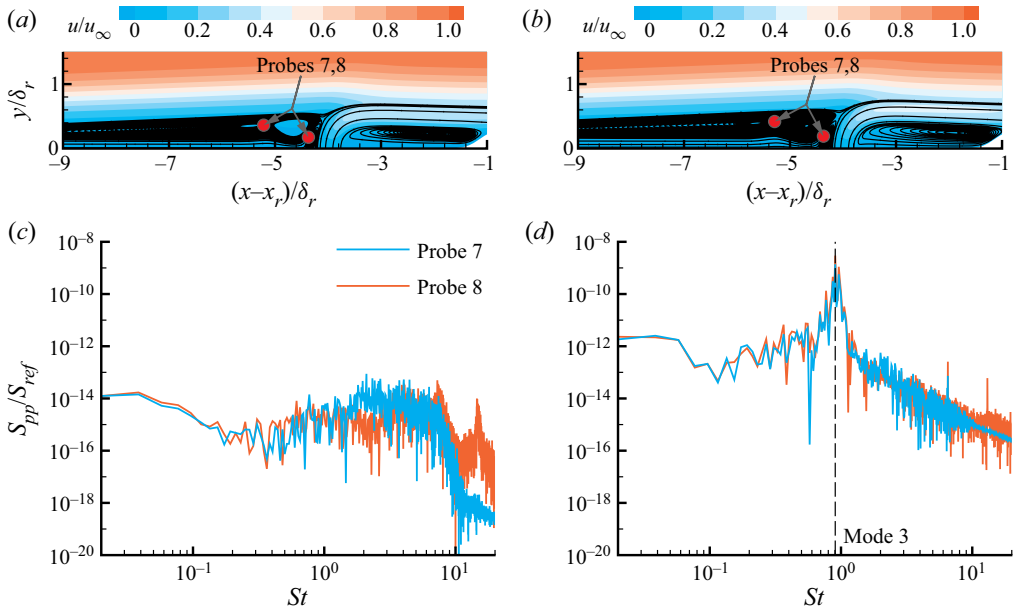


Figure 26. Separation zone at the upstream region of the blowing slot in (*a*,*c*) case $X_{-4}V_{18}$ and (*b*,*d*) $X_{-4}V_{20}$: (*a*,*b*) streamwise velocity profiles on the symmetry plane (black lines are in-plane streamlines), and (*c*,*d*) PSD results.

dominant frequency of the spectrum. As a result, the unstable mode 1 does not appear in the downstream region, and there exists no obvious dominant mode at probe 6. The flow freezing operation proves that mode 3 originates from the separation zone upstream of the blowing slot, and it is the key factor for the transition of cases with upstream-positioned strong blowing.

To get more features of mode 3, modes 1 and 3 extracted by DMD from case $X_{-4}V_{20}$ are reconstructed in figure 28. As demonstrated in figure 28(*a*), the distribution of pressure fluctuation amplitude of mode 1 in case $X_{-4}V_{20}$ shows a similar symmetry as in case V_0. Meanwhile, mode 3 presents significant asymmetry, which means that it may contain the sinuous mode related to the instability of the lateral shear layer (De Tullio *et al.* 2013).

Finally, cases with downstream-positioned strong wall blowing are analysed. Flow structures in the region near the roughness element for cases X_4V_{23} and X_4V_{25} are visualized in figure 29. In both cases, the separation zone upstream of the blowing slot is so large that the roughness element is totally immersed in it, and thus the vortex system in the separation zone is blocked by the roughness element and forms complex structures (see figure 29*a*,*b*). For streamwise vortices generated from the roughness element (horseshoe vortex and counter-rotating vortex pair), the effect of stretching provided by downstream-positioned strong wall blowing is much stronger than dissipation (see figure 29*e*,*f*). Therefore, streamwise vortices are strengthened with increasing blowing intensity (see figure 29*c*,*d*). Moreover, these streamwise vortices in the wake are lifted far away from the wall, and a shear layer subsequently forms under the vortex structures (see figure 29*g*,*h*). Similar to case $X_{-4}V_{20}$, the flow structure of case X_4V_{25} is more complicated than in case X_4V_{23} at $x - x_r = 12\delta_r$ because the wake flow becomes unstable. Figure 29(*j*) indicates that the velocity fluctuation grows most rapidly at the position of the shear layer in this stage.

https://doi.org/10.1017/jfm.2021.448 Published online by Cambridge University Press

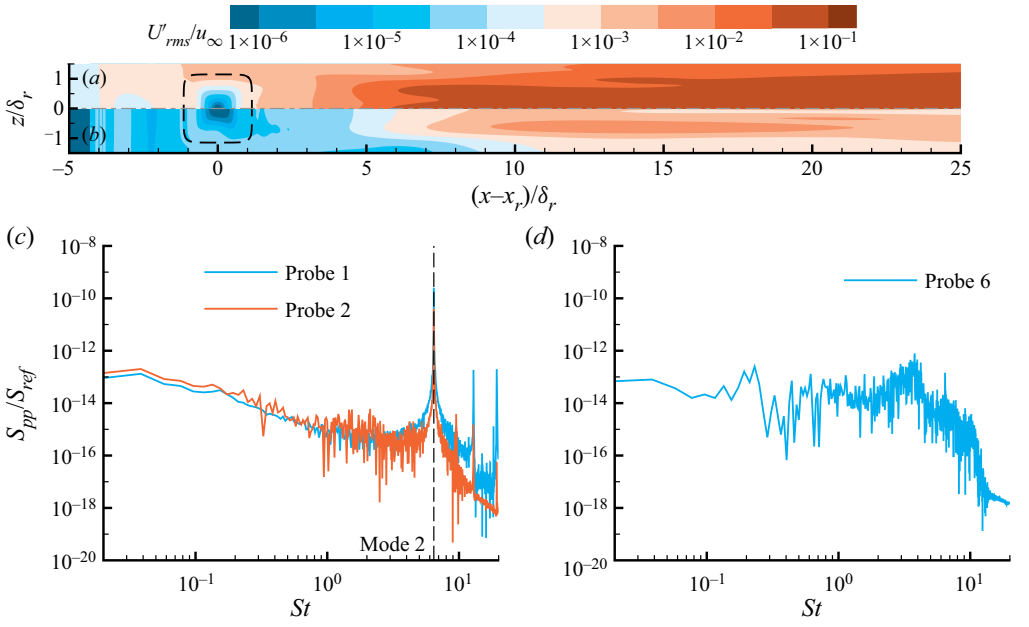


Figure 27. Flow freezing operation: (*a*,*b*) comparison of velocity fluctuation distributions at $y = k_r$ between (*a*) case $X_{-4}V_{20}$ and (*b*) case $X_{-4}V_{20}$ with the flow freezing operation (the dashed line indicates the roughness shape at the height of $k_r/2$); and PSD results for case $X_{-4}V_{20}$ with the flow freezing operation at (*c*) upstream region and (*d*) $x - x_r = 6\delta_r$.

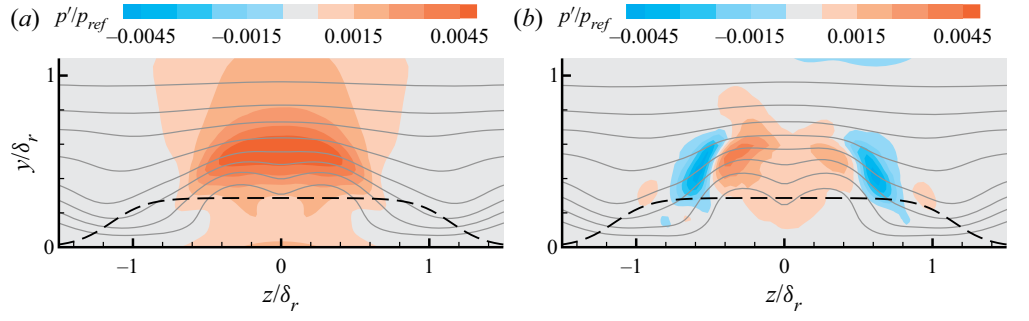


Figure 28. Reconstructions of (*a*) mode 1 at $x - x_r = 7\delta_r$ and (*b*) mode 3 at $x - x_r = 8\delta_r$. (The grey solid lines are isolines of u with the same value set, and the black dashed line indicates the projection of roughness.)

Following the analyses of other cases above, PSD results for the upstream and downstream regions of both cases are plotted in figure 30. As shown in figure 29, probe 9 is located between the roughness element and the blowing slot, and probe 10 is placed at $x - x_r = 12\delta_r$. The results in figure 30(*a*,*b*) suggest that there exists a very low-frequency ingredient, and therefore a much longer signal is adopted for PSD analysis of both cases. It can be observed that there is no dominant unstable mode in the medium- or high-frequency band at the upstream region. Instead, a very low-frequency unstable mode (named mode 4) is obvious at probes 1, 2 and 9 in both cases. In the downstream region, mode 4 maintains its amplitude. In the meantime, mode 1 grows rapidly and becomes the dominant unstable

https://doi.org/10.1017/jfm.2021.448 Published online by Cambridge University Press

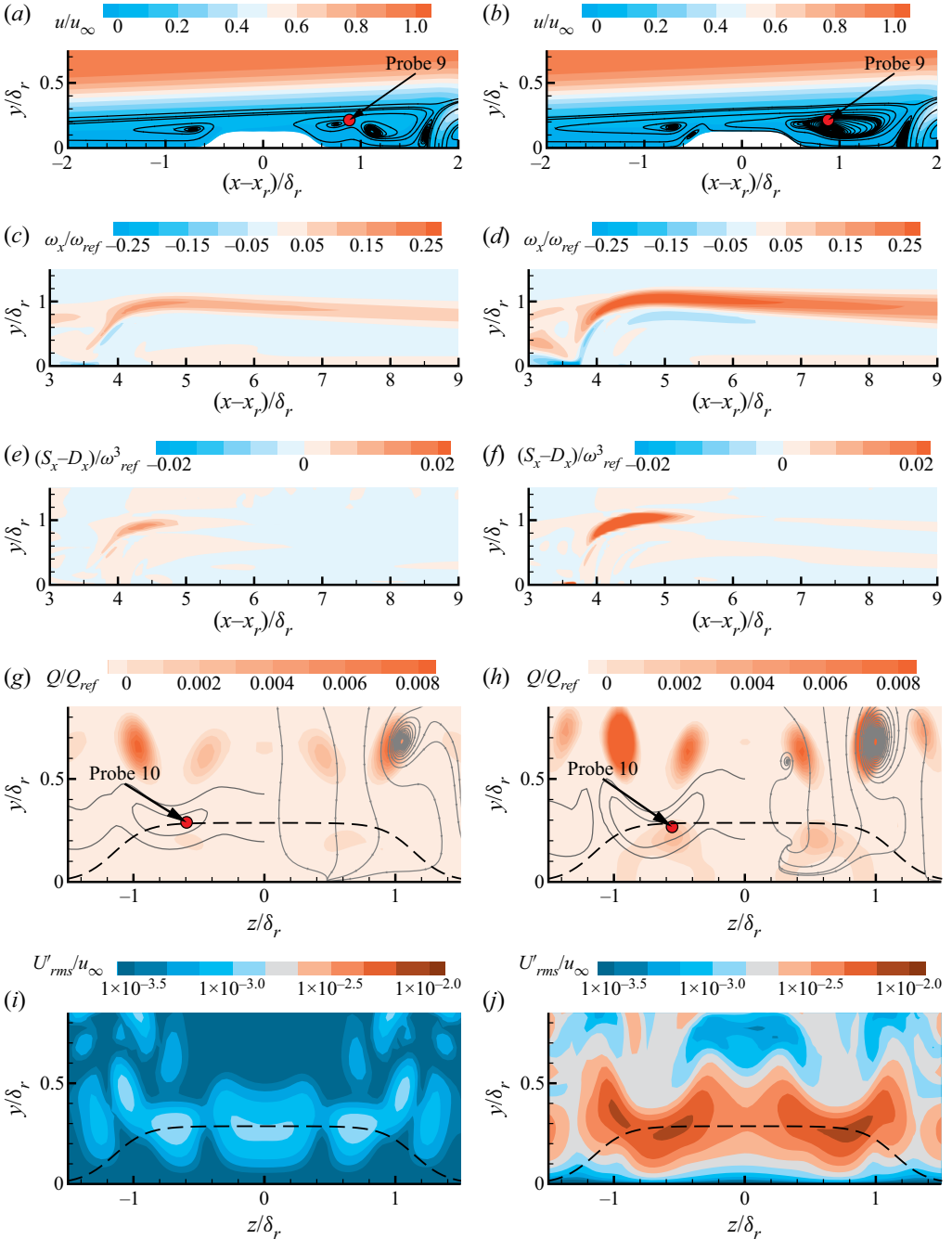


Figure 29. Flow visualization of (*a*,*c*,*e*,*g*,*i*) case X_4V_{23} and (*b*,*d*,*f*,*h*,*j*) case X_4V_{25}: (*a*,*b*) streamwise velocity profiles at the symmetry plane (black lines are in-plane streamlines), (*c*,*d*) profiles of streamwise vorticity at $z=-0.9\delta_r$, (*e*,*f*) profiles of vorticity transportation $(S_x-D_x)/S_{ref}$ at $z=-0.9\delta_r$, (*g*,*h*) slices of the Q criterion at $x-x_r=12\delta_r$ (the dark grey solid lines on the left half are isolines of u_s with the same value set and the light grey lines on the right are in-plane streamlines), and (*i*,*j*) slices of the velocity fluctuation at $x-x_r=12\delta_r$ (the black dashed line indicates the projection of roughness).

https://doi.org/10.1017/jfm.2021.448 Published online by Cambridge University Press

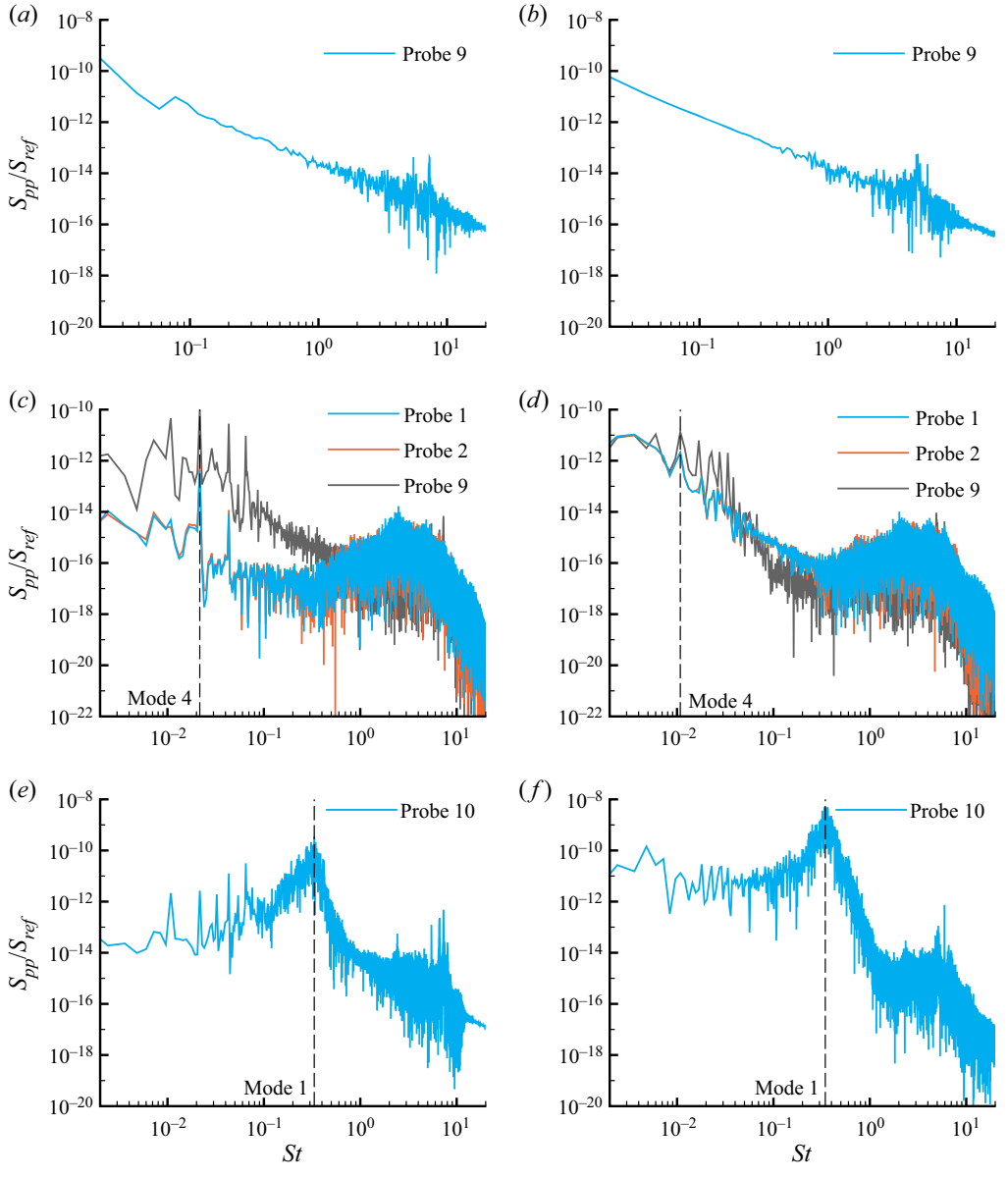


Figure 30. PSD results of pressure fluctuations for (*a*,*c*,*e*) case X_4V_{23} and (*b*,*d*,*f*) case X_4V_{25} at (*a–d*) the upstream region of the blowing slot and (*e*,*f*) $x - x_r = 12\delta_r$.

mode at probe 10. Similar to cases with upstream-positioned strong wall blowing, we can assume that the transition occurring in these two cases can be attributed to mode 4.

Two different cases with flow freezing operations are simulated to test our assumption. For case $X_4V_{25}F_1$, the region $x - x_r \leq -0.777\delta_r$ (upstream region of the roughness element) is frozen, and for case $X_4V_{25}F_2$, the freezing region is $x - x_r \leq 4.287\delta_r$ (blowing slot and the upstream region of it). It can be observed from figure 31(*e*) that mode 4 still exists with the upstream region of the roughness element being frozen. Meanwhile, in case $X_4V_{25}F_2$, the unstable mode 4 totally disappears. This suggests that the very low-frequency

https://doi.org/10.1017/jfm.2021.448 Published online by Cambridge University Press

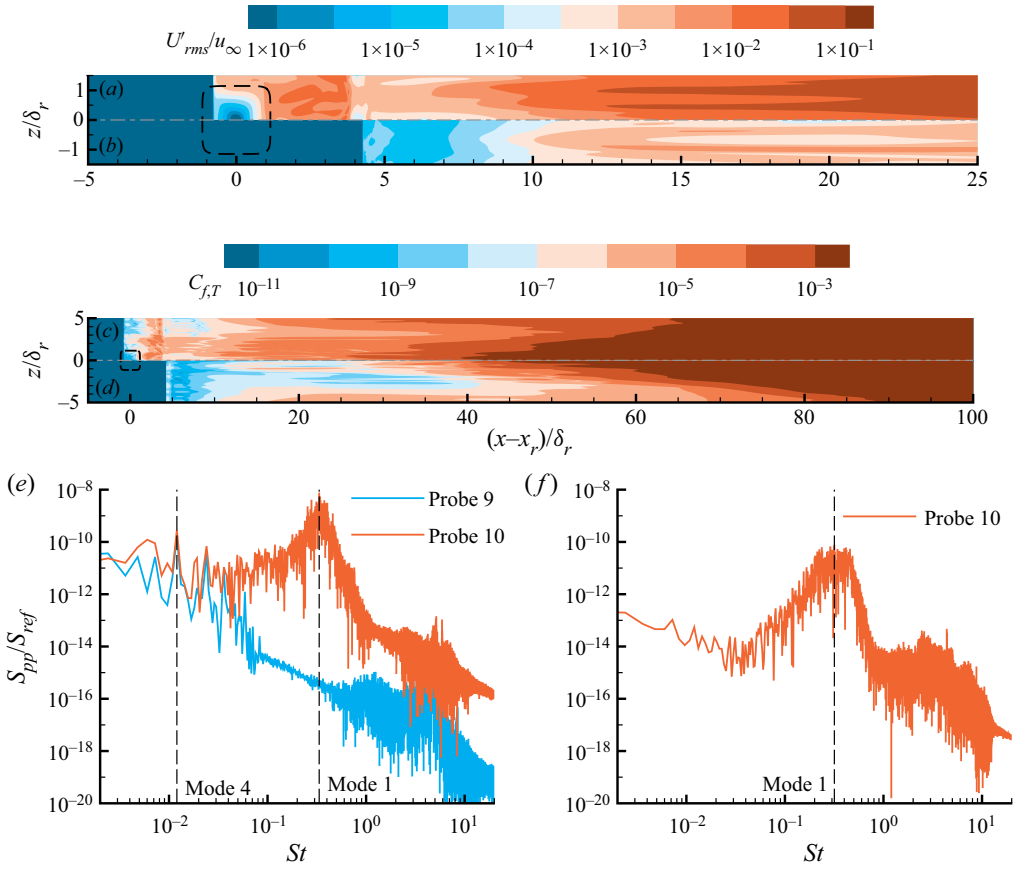


Figure 31. Flow freezing operations: comparison of (*a*,*b*) velocity fluctuation distributions at $y = k_r$ and (*c*,*d*) $C_{f,T}$ distributions between (*a*,*c*) case $X_4V_{25}F_1$ and (*b*,*d*) $X_4V_{25}F_2$ (the dashed line indicates the roughness shape at the height of $k_r/2$); and PSD results for (*e*) $X_4V_{25}F_1$ and (*f*) case $X_4V_{25}F_2$.

mode 4 is generated from the separation zone between the roughness element and the blowing slot. Similar to cases X_4V_{23} and X_4V_{25}, mode 1 is the dominant unstable mode in the downstream region. Owing to the flow freezing operation, the amplitude of mode 1 at probe 10 in case $X_4V_{25}F_2$ is even smaller than that in case X_4V_{23}. However, as demonstrated in figure 31(*d*), the transition still occurs in the downstream region of case $X_4V_{25}F_2$ with only a slight delay due to the lower initial disturbance level downstream of the blowing slot. These results indicate that the very low-frequency mode 4 is not the key factor to determine whether the transition occurs. Instead, it only provides an initial disturbance level for the transition process downstream. The main source of unsteadiness in the transition process of case X_4V_{25} is the wake structure in the downstream region of the blowing slot.

For further confirmation, a comparison between slices of case X_4V_{23} and case $X_4V_{25}F_2$ at $x - x_r = 24\delta_r$ and $36\delta_r$ is illustrated in figure 32. While the shear layer in the wake is already relaxed at $x - x_r = 24\delta_r$, with the reattachment of the flow blown out from the slot, streamwise vortices pushed away by wall blowing return to the near-wall region and induce significant distortion of the spanwise boundary layer profile at this position. As analysed in figure 29, streamwise vortices in the wake become stronger with the increase in the blowing intensity. Meanwhile, due to the freezing of the upstream flow field, the

https://doi.org/10.1017/jfm.2021.448 Published online by Cambridge University Press

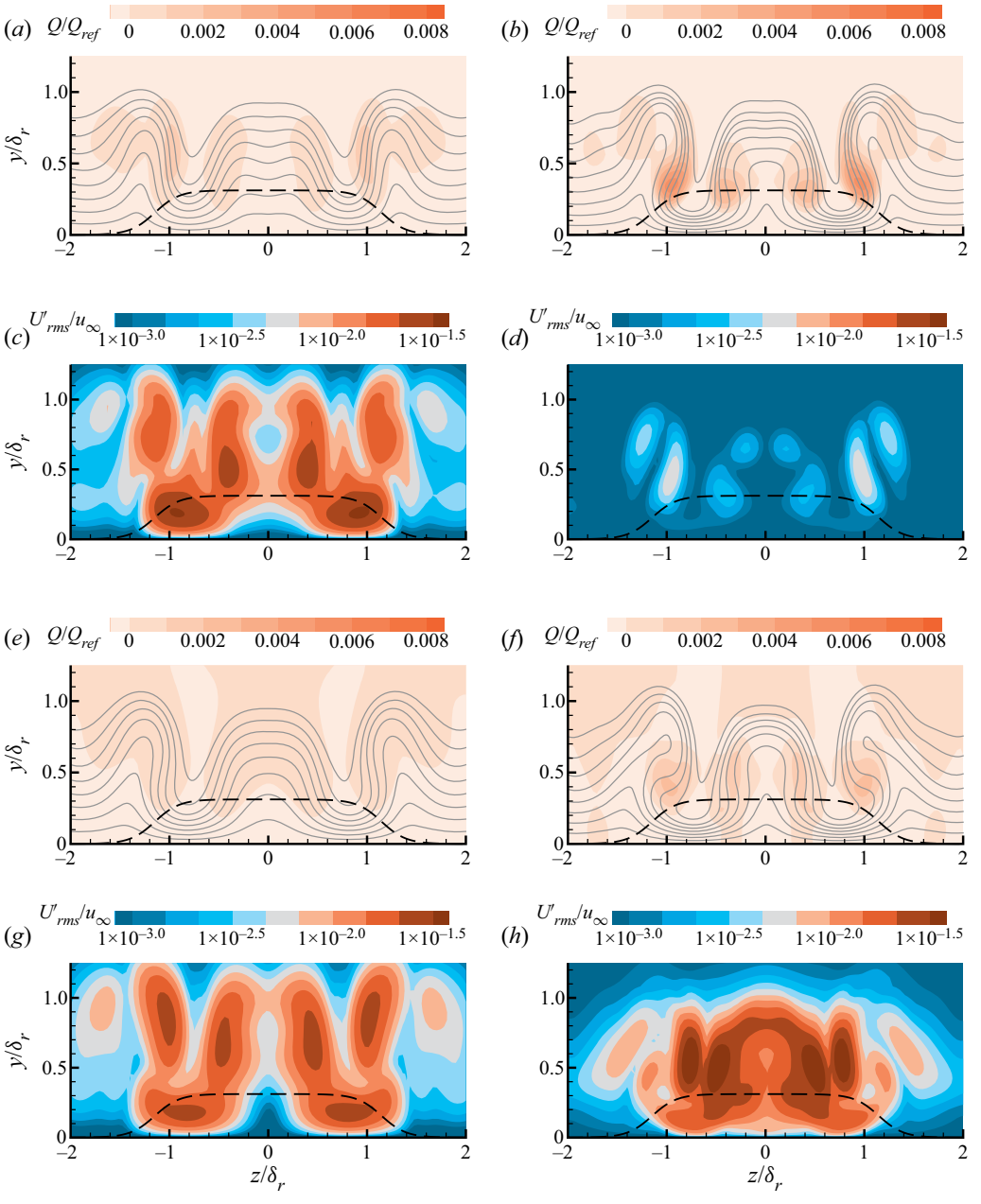


Figure 32. Slices of (*a*,*c*,*e*,*g*) case X_4V_{23} and (*b*,*d*,*f*,*h*) case $X_4V_{25}F_2$ at (*a–d*) $x - x_r = 24\delta_r$ and (*e–h*) $x - x_r = 36\delta_r$ coloured with (*a*,*b*,*e*,*f*) the non-dimensional Q criterion and (*c*,*d*,*g*,*h*) the streamwise velocity fluctuation. (The grey lines are in-plane streamlines, and the black dashed line indicates the projection of roughness.)

initial disturbance level of case $X_4V_{25}F_2$ at $x - x_r = 24\delta_r$ is much lower than that of case X_4V_{23}. At $x - x_r = 36\delta_r$, the disturbance level of case X_4V_{23} changes little, and the streamwise vorticity is largely dissipated and cannot provide continuous growth for disturbance. However, the stronger streamwise vortices in the wake of case $X_4V_{25}F_2$ lead to a rapid growth of disturbance, and the velocity fluctuation at $x - x_r = 36\delta_r$ is already

https://doi.org/10.1017/jfm.2021.448 Published online by Cambridge University Press

stronger than that in case X_4V_{23}. Moreover, figure 32(f,h) shows that the disturbance grows most rapidly at positions where the spanwise vorticity is slanted and converted into the wall-normal type by streamwise vortices. This agrees with the description of the lift-up mechanism (Landahl 1980; Brandt 2014).

4. Conclusion

In this paper, the control effect of two-dimensional upstream- or downstream-positioned blowing with various intensities on a three-dimensional discrete roughness-induced transition is investigated using DNS.

The transition mechanism of flow past the smooth-edged roughness element is first analysed. As proposed by Subbareddy *et al.* (2014), typical structures in the flow field consist of (1) the horseshoe vortex system formed in the upstream separation zone, (2) the upstream shockwave system and (3) the downstream separated shear layer/counter-rotating vortex system. PSD results of pressure fluctuations at these three structures show that the dominant unstable modes in the upstream or downstream region of the roughness element are different. The flow freezing operation proves that the main source of unsteadiness in the transition process is the separated shear layer/counter-rotating vortex pair interaction, which is also confirmed by SPOD and DMD analyses. The separated shear layer is bent by the counter-rotating vortex pair, and the interaction between them induces a rapid disturbance growth at the position of the shear layer.

With the existence of weak wall blowing, the skin friction drag is largely reduced, and FIK decomposition reveals that the reduction is accomplished by delaying the laminar–turbulent transition induced by the roughness element. Visualization of the flow field demonstrates that the upstream-positioned blowing is able to diminish the strength of main structures in the wake by lifting the inflow boundary layer and decreasing the value of the effective roughness Reynolds number. In regard to downstream-positioned weak wall blowing, it takes effect by weakening the counter-rotating vortex pair and inhibiting the interaction of the separated shear layer/counter-rotating vortex system. Vorticity transportation analysis suggests that this is achieved by increasing the dissipation for streamwise vorticity and converting some of it into spanwise vorticity.

While the enhancement of wall blowing can significantly reduce friction drag and delay transition, this trend cannot always continue. In contrast, the wall blowing can induce unsteadiness and promote transition when it is strong enough. In upstream-positioned strong wall blowing cases, it can be observed from the PSD results that there exists a new unstable mode in both upstream and downstream regions. The flow freezing operation indicates that the new unstable mode originates from the separation zone upstream of the blowing slot, and it is the key factor in the transition process of cases with upstream-positioned strong blowing because transition would not occur without it. However, the mechanism for downstream-positioned strong wall blowing cases is different. As demonstrated in the PSD results, a very low-frequency unstable mode is generated from the separation bubble between the roughness element and the blowing slot. However, it is not the primary cause of transition in these cases. Despite the separation bubble being frozen, transition still occurs downstream with only a slight delay. The very low-frequency mode only provides an initial disturbance level for the transition process. The main source of unsteadiness in cases with downstream-positioned strong blowing is the distortion of the boundary layer profile in the wake behind the blowing slot.

Acknowledgements. The authors would like to acknowledge Professor X. Li from the Institute of Mechanics, Chinese Academy of Sciences, for the finite-difference code OpenCFD.

https://doi.org/10.1017/jfm.2021.448 Published online by Cambridge University Press

Declaration of interests. The authors report no conflict of interest.

Funding. This work is supported by grants from the National Numerical Wind Tunnel Project of China (No. NNW2019ZT1-A03), the National Natural Science Foundation of China (Nos. 11721202 and 11902367) and the Academic Excellence Foundation of BUAA for PhD Students.

Author ORCIDs.
Yuhan Lu https://orcid.org/0000-0002-6276-0385;
Fanzhi Zeng https://orcid.org/0000-0002-6771-9664;
Zaijie Liu https://orcid.org/0000-0002-1540-6666;
Chao Yan https://orcid.org/0000-0002-2691-7955.

References

Bajura, R.A. & Catalano, M.R. 1975 Transition in a two-dimensional plane wall jet. *J. Fluid Mech.* **70** (4), 773–799.

Baker, C.J. 1979 The laminar horseshoe vortex. *J. Fluid Mech.* **95** (2), 347–367.

Balakumar, P. & Kegerise, M. 2016 Roughness-induced transition in a supersonic boundary layer. *AIAA J.* **54** (8), 2322–2337.

Bernardini, M., Pirozzoli, S., Orlandi, P. & Lele, S.K. 2014 Parameterization of boundary-layer transition induced by isolated roughness elements. *AIAA J.* **52** (10), 2261–2269.

Brandt, L. 2014 The lift-up effect: the linear mechanism behind transition and turbulence in shear flows. *Eur. J. Mech. (*B*/Fluids)* **47**, 80–96.

Brown, G.L., Lee, M. -K. & Moser, R.D. 2015 Vorticity transport: the transfer of viscous stress to Reynolds stress in turbulent channel flow. In *Proceedings of TSFP-9*, pp. 673–678. TSFP Organizing Committee.

Bucci, M.A., Puckert, D.K., Andriano, C., Loiseau, J.-C., Cherubini, S., Robinet, J.-C. & Rist, U. 2018 Roughness-induced transition by quasi-resonance of a varicose global mode. *J. Fluid Mech.* **836**, 167–191.

Butcher, J.C. 2003 *Numerical Methods for Ordinary Differential Equations*, 2nd edn. Wiley.

Chou, A., Kegerise, M.A. & King, R.A. 2020 Transition induced by streamwise arrays of roughness elements on a flat plate in mach 3.5 flow. *J. Fluid Mech.* **888**, A21.

Citro, V., Giannetti, F., Luchini, P. & Auteri, F. 2015 Global stability and sensitivity analysis of boundary-layer flows past a hemispherical roughness element. *Phys. Fluids* **27** (8), 084110.

Coles, D. 1956 The law of the wake in the turbulent boundary layer. *J. Fluid Mech.* **1** (2), 191–226.

De Tullio, N., Paredes, P., Sandham, N.D. & Theofilis, V. 2013 Laminar–turbulent transition induced by a discrete roughness element in a supersonic boundary layer. *J. Fluid Mech.* **735**, 613–646.

Deng, X.-G., Mao, M.-L., Tu, G.-H., Liu, H.-Y. & Zhang, H.-X. 2011 Geometric conservation law and applications to high-order finite difference schemes with stationary grids. *J. Comput. Phys.* **230** (4), 1100–1115.

Downs, R.S.III, White, E.B. & Denissen, N.A. 2008 Transient growth and transition induced by random distributed roughness. *AIAA J.* **46** (2), 451–462.

van Driest, E.R. 1951 Turbulent boundary layer in compressible fluids. *J. Aeronaut. Sci.* **18** (3), 145–160.

Ergin, F.G. & White, E.B. 2006 Unsteady and transitional flows behind roughness elements. *AIAA J.* **44** (11), 2504–2514.

Estruch-Samper, D., Hillier, R., Vanstone, L. & Ganapathisubramani, B. 2017 Effect of isolated roughness element height on high-speed laminar–turbulent transition. *J. Fluid Mech.* **818**, R1.

Fukagata, K., Iwamoto, K. & Kasagi, N. 2002 Contribution of Reynolds stress distribution to the skin friction in wall-bounded flows. *Phys. Fluids* **14** (11), L73–L76.

Gomez, T., Flutet, V. & Sagaut, P. 2009 Contribution of Reynolds stress distribution to the skin friction in compressible turbulent channel flows. *Phys. Rev.* E **79** (3), 035301.

Gregory, N. & Walker, W.S. 1956 The effect on transition of isolated surface excrescences in the boundary layer. *Tech. Rep.* Aeronautical Research Council, Ministry of Supply.

Hamed, A.M., Sadowski, M., Zhang, Z. & Chamorro, L.P. 2016 Transition to turbulence over 2D and 3D periodic large-scale roughnesses. *J. Fluid Mech.* **804**, R6.

Hunt, J.C.R., Wray, A.A. & Moin, P. 1988 Eddies, streams, and convergence zones in turbulent flows. In *Proceedings of the 1998 Summer Program*, pp. 193–208. Stanford University.

Jiang, G.-S. & Shu, C.-W. 1996 Efficient implementation of weighted ENO schemes. *J. Comput. Phys.* **126** (1), 202–228.

https://doi.org/10.1017/jfm.2021.448 Published online by Cambridge University Press

JOVANOVIĆ, M.R., SCHMID, P.J. & NICHOLS, J.W. 2014 Sparsity-promoting dynamic mode decomposition. *Phys. Fluids* **26** (2), 024103.

KENDALL, J.M. 1981 Study of the effect of free-stream turbulence upon disturbances in the pre-transitional laminar boundary layer. *Tech. Rep.* AFWAL.

KLEBANOFF, P.S., CLEVELAND, W.G. & TIDSTROM, K.D. 1992 On the evolution of a turbulent boundary layer induced by a three-dimensional roughness element. *J. Fluid Mech.* **237**, 101–187.

KOBAYASHI, R., FUKUNISHI, Y., NISHIKAWA, T. & KATO, T. 1994 The receptivity of flat-plate boundary-layers with two-dimensional roughness elements to freestream sound and its control. In *Laminar–Turbulent Transition*, pp. 507–514. IUTAM.

KUESTER, M.S. & WHITE, E.B. 2015 Roughness receptivity and shielding in a flat plate boundary layer. *J. Fluid Mech.* **777**, 430–460.

LANDAHL, M.T. 1980 A note on an algebraic instability of inviscid parallel shear flows. *J. Fluid Mech.* **98** (2), 243–251.

LI, X.-L., FU, D.-X., MA, Y.-W. & GAO, H. 2009 Acoustic calculation for supersonic turbulent boundary layer flow. *Chin. Phys. Lett.* **26** (9), 1–4.

LI, X.-L., FU, D.-X., MA, Y.-W. & LIANG, X. 2010 Development of high accuracy CFD software Hoam-OpenCFD. *e-Sci. Technol. Appl.* **1**, 53–59.

LIN, T.C. 2008 Influence of laminar boundary-layer transition on entry vehicle designs. *J. Spacecr. Rockets* **45** (2), 165–175.

LOISEAU, J.-C., ROBINET, J.-C., CHERUBINI, S. & LERICHE, E. 2014 Investigation of the roughness-induced transition: global stability analyses and direct numerical simulations. *J. Fluid Mech.* **760**, 175–211.

LU, Y.-H., LIU, H.-K., LIU, Z.-J. & YAN, C. 2020*a* Assessment and parameterization of upstream shielding effect in quasi-roughness induced transition with direct numerical simulations. *Aerosp. Sci. Technol.* **100**, 105824.

LU, Y.-H., LIU, H.-K., LIU, Z.-J. & YAN, C. 2020*b* Investigation and parameterization of transition shielding in roughness-disturbed boundary layer with direct numerical simulations. *Phys. Fluids* **32** (7), 074110.

LUCHINI, P. 2000 Reynolds-number-independent instability of the boundary layer over a flat surface: optimal perturbations. *J. Fluid Mech.* **404**, 289–309.

LUMLEY, J.L. 1970 *Stochastic Tools in Turbulence*. Academic Press.

MARTIN, M.P., TAYLOR, E.M., WU, M. & WEIRS, V.G. 2006 A bandwidth-optimized WENO scheme for the effective direct numerical simulation of compressible turbulence. *J. Comput. Phys.* **220** (1), 270–289.

MORI, E., QUADRIO, M. & FUKAGATA, K. 2017 Turbulent drag reduction by uniform blowing over a two-dimensional roughness. *Flow Turbul. Combust.* **99**, 765–785.

MUPPIDI, S. & MAHESH, K. 2012 Direct numerical simulations of roughness-induced transition in supersonic boundary layers. *J. Fluid Mech.* **693**, 28–56.

PIROZZOLI, S., GRASSO, F. & D'ANDREA, A. 2001 Interaction of a shock wave with two counter-rotating vortices: shock dynamics and sound production. *Phys. Fluids* **13** (11), 3460–3481.

PIROZZOLI, S., GRASSO, F. & GATSKI, T.B. 2004 Direct numerical simulation and analysis of a spatially evolving supersonic turbulent boundary layer at $M = 2.25$. *Phys. Fluids* **16** (3), 530–545.

POINSOT, T.J. & LELE, S.K. 1992 Boundary conditions for direct simulations of compressible viscous flows. *J. Comput. Phys.* **101** (1), 104–129.

PUCKERT, D.K. & RIST, U. 2018 Experiments on critical Reynolds number and global instability in roughness-induced laminar–turbulent transition. *J. Fluid Mech.* **844**, 878–904.

PUCKERT, D.K. & RIST, U. 2019 Experimental observation of frequency lock-in of roughness-induced instabilities in a laminar boundary layer. *J. Fluid Mech.* **870**, 680–697.

RESHOTKO, E. 2001 Transient growth: a factor in bypass transition. *Phys. Fluids* **13** (5), 1067–1075.

ROWLEY, C.W., MEZIĆ, I., BAGHERI, S. & SCHLATTER, P. 2009 Spectral analysis of nonlinear flows. *J. Fluid Mech.* **641**, 115–127.

SAYADI, T. & SCHMID, P.J. 2016 Parallel data-driven decomposition algorithm for large-scale datasets: with application to transitional boundary layers. *Theor. Comput. Fluid Dyn.* **30**, 415–428.

SCHMID, P.J. 2010 Dynamic mode decomposition of numerical and experimental data. *J. Fluid Mech.* **656**, 5–28.

SCHNEIDER, S.P. 2015 Developing mechanism-based methods for estimating hypersonic boundary-layer transition in flight: the role of quiet tunnels. *Prog. Aeosp. Sci.* **72**, 17–29.

SEMPER, M.T. & BOWERSOX, R.D.W. 2017 Tripping of a hypersonic low-Reynolds-number boundary layer. *AIAA J.* **55** (3), 808–817.

https://doi.org/10.1017/jfm.2021.448 Published online by Cambridge University Press

SHARMA, A., DREWS, S., KUESTER, M.S., GOLDSTEIN, D.B. & WHITE, E.B. 2014 Evolution of disturbances due to distributed surface roughness in laminar boundary layers. *AIAA Paper* 2014-0235. AIAA.

SHARMA, S., SHADLOO, M.S., HADJADJ, A. & KLOKER, M.J. 2019 Control of oblique-type breakdown in a supersonic boundary layer employing streaks. *J. Fluid Mech.* **873**, 1072–1089.

SHRESTHA, P. & CANDLER, G.V. 2019 Direct numerical simulation of high-speed transition due to roughness elements. *J. Fluid Mech.* **868**, 762–788.

SMITH, A.M.O. & CLUTTER, D.W. 1959 The smallest height of roughness capable of affecting boundary-layer transition. *J. Aeronaut. Sci.* **26** (4), 229–256.

STEGER, J.L. & WARMING, R.F. 1981 Flux vector splitting of the inviscid gasdynamic equations with application to finite-difference methods. *J. Comput. Phys.* **40** (2), 263–293.

STEWARTSON, K. 1964 *The Theory of Laminar Boundary Layers in Compressible Fluids*. Oxford University Press.

SUBBAREDDY, P.K., BARTKOWICZ, M.D. & CANDLER, G.V. 2014 Direct numerical simulation of high-speed transition due to an isolated roughness element. *J. Fluid Mech.* **748**, 848–878.

SURYANARAYANAN, S., GOLDSTEIN, D.B., BERGER, A.R., WHITE, E.B. & BROWN, G.L. 2020 Mechanisms of roughness-induced boundary-layer transition control by shielding. *AIAA J.* **58** (7), 2951–2963.

SURYANARAYANAN, S., GOLDSTEIN, D.B., BROWN, G.L., BERGER, A.R. & WHITE, E.B. 2017 On the mechanics and control of boundary layer transition induced by discrete roughness elements. *AIAA Paper* 2017-0307. AIAA.

TOWNE, A., SCHMIDT, O.T. & COLONIUS, T. 2018 Spectral proper orthogonal decomposition and its relationship to dynamic mode decomposition and resolvent analysis. *J. Fluid Mech.* **847**, 821–867.

TSUJI, Y., MORIKAWA, Y., NAGATANI, T. & SAKOU, M. 1977 The stability of a two-dimensional wall jet. *Aeronaut. Q.* **28** (4), 235–246.

WERNZ, S. & FASEL, H. 1997 Numerical investigation of forced transitional wall jets. *AIAA Paper* 1997-2022. AIAA.

WHITE, E.B. 2002 Transient growth of stationary disturbances in a flat plate boundary layer. *Phys. Fluids* **14** (12), 4429–4439.

WHITE, F.M. & CHRISTOPH, G.H. 1972 A simple theory for the two-dimensional compressible turbulent boundary layer. *Trans. ASME J. Basic Engng* **94** (3), 636–642.

WHITE, E.B., RICE, J.M. & ERGIN, F.G. 2005 Receptivity of stationary transient disturbances to surface roughness. *Phys. Fluids* **17** (6), 064109.

https://doi.org/10.1017/jfm.2021.448 Published online by Cambridge University Press